Journal of Computational Physics 234 (2013) 172–198

Contents lists available at SciVerse ScienceDirect

Journal of Computational Physics

journal homepage: www.elsevier.com/locate/jcp

Discrete Calderon's projections on parallelepipeds and their application to computing exterior magnetic fields for FRC plasmas ☆

E. Kansa [a], U. Shumlak [a,b], S. Tsynkov [a,c,*]

[a] Computational Sciences, LLC, 8000 Madison Blvd., Madison, AL 35758-2035, USA
[b] Aerospace & Energetics Research Program, University of Washington, Box 352250, Seattle, WA 98195, USA
[c] Department of Mathematics, North Carolina State University, Box 8205, Raleigh, NC 27695, USA

ARTICLE INFO

Article history:
Received 23 July 2012
Received in revised form 18 September 2012
Accepted 20 September 2012
Available online 13 October 2012

Keywords:
Field reversed configuration (FRC)
Single fluid magnetohydrodynamics (MHD)
Quasi-static magnetic field
Artificial boundary condition (ABC)
The method of difference potentials
Calderon's potentials and projections
Boundary equations with projections

ABSTRACT

Confining dense plasma in a field reversed configuration (FRC) is considered a promising approach to fusion. Numerical simulation of this process requires setting artificial boundary conditions (ABCs) for the magnetic field because whereas the plasma itself occupies a bounded region (within the FRC coils), the field extends from this region all the way to infinity. If the plasma is modeled using single fluid magnetohydrodynamics (MHD), then the exterior magnetic field can be considered quasi-static. This field has a scalar potential governed by the Laplace equation. The quasi-static ABC for the magnetic field is obtained using the method of difference potentials, in the form of a discrete Calderon boundary equation with projection on the artificial boundary shaped as a parallelepiped. The Calderon projection itself is computed by convolution with the discrete fundamental solution on the three-dimensional Cartesian grid.

1. Introduction

1.1. Single fluid magnetohydrodynamics

Single fluid magnetohydrodynamics (MHD) is a mathematical model that describes the motion of a charge-neutral electrically conductive fluid. As it applies to plasma, which is a quasi-neutral composition of positively and negatively charged species of particles (ions and electrons, respectively), the single fluid MHD neglects the mass of the electrons (since they are much lighter than the ions) and interprets the macroscopic velocity of the fluid $\boldsymbol{u}$ as that of the ions. The inviscid momentum equation then becomes:

$$m_i n \frac{d\boldsymbol{u}}{dt} + \operatorname{grad} p = \frac{1}{c}\boldsymbol{j} \times \boldsymbol{B}, \tag{1}$$

where m_i is the ion mass, n is the number density of singly charged ions, p is the pressure, $\boldsymbol{j}$ is the density of the electric current, $\boldsymbol{B}$ is the magnetic field, and c is the speed of light. The term on the right-hand side of Eq. (1) is known as the Lorentz force.

Eq. (1) is supplemented by the equation of conservation of mass:

☆ Work supported by AFRL under contract No. FA945109C0165.

* Corresponding author at: Department of Mathematics, North Carolina State University, Box 8205, Raleigh, NC 27695, USA. Tel.: +1 919 515 1877; fax : +1 919 513 7336.

E-mail addresses: edwardjkansa@netzero.com (E. Kansa), shumlak@uw.edu (U. Shumlak), tsynkov@math.ncsu.edu (S. Tsynkov).

0021-9991/$ - see front matter © 2012 Elsevier Inc. All rights reserved.
http://dx.doi.org/10.1016/j.jcp.2012.09.033

$$\frac{\partial n}{\partial t} + \operatorname{div} n\boldsymbol{u} = 0, \tag{2}$$

as well as by the Maxwell equations of electrodynamics. The Maxwell equations are simplified though. First, we neglect the displacement current in the Ampère law (assuming that the macroscopic speeds are much slower than the speed of light), which yields:

$$\operatorname{curl} \boldsymbol{B} = \frac{4\pi}{c}\boldsymbol{j}. \tag{3}$$

Second, let $\tilde{\boldsymbol{E}}$ be the electric field in the coordinate system that moves with the fluid ($|\boldsymbol{u}| \ll c$):

$$\tilde{\boldsymbol{E}} = \boldsymbol{E} + \frac{1}{c}\boldsymbol{u} \times \boldsymbol{B}, \tag{4}$$

and let σ denote the electric conductivity of the plasma. Employing the classical Ohm law, we can write $\boldsymbol{j} = \sigma\tilde{\boldsymbol{E}}$, and from Eqs. (4) and (3) derive:

$$\boldsymbol{E} = \frac{c}{4\pi\sigma}\operatorname{curl} \boldsymbol{B} - \frac{1}{c}\boldsymbol{u} \times \boldsymbol{B}.$$

Substituting this expression for $\boldsymbol{E}$ into the Faraday law

$$\frac{1}{c}\frac{\partial \boldsymbol{B}}{\partial t} = -\operatorname{curl} \boldsymbol{E}, \tag{5}$$

we obtain

$$\frac{\partial \boldsymbol{B}}{\partial t} = \operatorname{curl}[\boldsymbol{u} \times \boldsymbol{B}] - \frac{c^2}{4\pi\sigma}(\operatorname{grad}\operatorname{div} \boldsymbol{B} - \Delta \boldsymbol{B}),$$

and using the Gauss law of magnetism

$$\operatorname{div} \boldsymbol{B} = 0, \tag{6}$$

we arrive at the equation of magnetic diffusion:

$$\frac{\partial \boldsymbol{B}}{\partial t} = \operatorname{curl}[\boldsymbol{u} \times \boldsymbol{B}] + \frac{c^2}{4\pi\sigma}\Delta \boldsymbol{B}, \tag{7}$$

for which the quantity $\frac{c^2}{4\pi\sigma}$ is called the magnetic diffusion coefficient. Eqs. (1), (2), (3), and (7) are main equations of the single fluid MHD. They, however, do not comprise a complete system unless supplemented by the energy equation (or heat transfer equation) and the equation of state. In many cases though, instead of the full energy equation one can use a simple polytropic relation between the pressure p and the concentration of particles n (e.g., adiabatic or isothermal).

The assumptions we made when deriving the single fluid MHD equations, which are neglecting the mass of the electrons, neglecting the displacement current, and assuming that the electric conductivity is constant, indicate that the resulting model should best describe the large scale and low frequency phenomena in plasma. A very important question then arises as to how to quantify the notions of "large scale" and "low frequency." We address some theoretical aspects of this question in Appendix A, and then provide specific quantitative estimates in Appendix B.

In Section 1.2 below, we describe the field reversed configuration (FRC) in plasma, which is considered a promising approach to fusion; in Section 1.3, we describe the *MACH3* code used for computing the FRCs; and in Section 1.4, we formulate the main problem for the current paper, which is the design of artificial boundary conditions for *MACH3*.

1.2. Field reversed configuration

The FRC is a magnetically confined plasma equilibrium that produces a compact toroid plasma shape. An axial magnetic field, produced by solenoidal coils, is embedded in a plasma. The magnetic field is quickly reversed which drives a toroidal or azimuthal plasma current. The magnetic field reconnects at the ends, and the poloidal magnetic field compresses the plasma axially and radially into a toroidal configuration where plasma pressure is balanced by magnetic field pressure and tension. The resulting equilibrium is an FRC.

The magnetic field of an FRC is the superposition of the field produced by the solenoid and the field produced by the plasma current. An exterior magnetic field extends over a large vacuum region (all the way out to infinity) beyond the plasma volume. Calculating the effect of the exterior magnetic field on the FRC without actually simulating the exterior domain represents a significant computational benefit, see Section 1.4.

The FRC equilibrium satisfies the momentum equation, Eq. (1), for static and steady-state conditions. The resulting force balance equation is given by

$$\operatorname{grad} p = \frac{1}{c}\boldsymbol{j} \times \boldsymbol{B} = \frac{1}{4\pi}\operatorname{curl} \boldsymbol{B} \times \boldsymbol{B}, \tag{8}$$

where the Ampère law (3) has been used to replace the current density. For axisymmetric equilibria, a poloidal magnetic flux function ψ can be introduced to define the poloidal magnetic field as

$$\boldsymbol{B} = \operatorname{grad}\psi \times \frac{\hat{\phi}}{r}, \tag{9}$$

where r is the radial coordinate and $\hat{\phi}$ is the unit vector in the azimuthal direction in a cylindrical coordinate system. Eq. (8) can then be expressed as

$$\Delta^*\psi = -4\pi r^2 \frac{dp}{d\psi}, \tag{10}$$

with the operator Δ^* is defined as

$$\Delta^* \equiv r\frac{\partial}{\partial r}\frac{1}{r}\frac{\partial}{\partial r} + \frac{\partial^2}{\partial z^2}.$$

Eq. (10) is the Grad–Shafranov equation, see [1,2], appropriate for an FRC.

The solution to Eq. (10) is found by specifying a functional form of the pressure $p(\psi)$, such that the pressure peak occurs at the magnetic axis defined as $\psi = 1$, and the pressure drops to a uniform background value at the magnetic separatrix defined as $\psi = 0$. For example,

$$p(\psi) = \begin{cases} p_{max}\psi^2 & \text{for} \quad \psi \geqslant 0, \\ p_{background} & \text{for} \quad \psi < 0. \end{cases} \tag{11}$$

The magnetic field external to the separatrix has $\psi < 0$.

Magnetic fields can confine plasmas since they exert a perpendicular force and since the perpendicular thermal conductivity is generally several orders of magnitude lower than parallel thermal conductivity. Improved confinement is achieved if no magnetic fields penetrate solid material surfaces. The FRC equilibrium is surrounded by solenoidal field coils that produce the axial magnetic field that provides the external radial force balance as required by the virial theorem [2]. These solenoidal field coils provide a cylindrical boundary that contains the FRC equilibrium. To prevent energy loss from the plasma to the solenoidal coils, an equilibrium is found such that $\boldsymbol{B}\cdot\boldsymbol{n} = 0$, where $\boldsymbol{n}$ is the unit normal to the boundary surface. Equivalently, $\psi = \psi_{net}$ along the boundary, where ψ_{net} is a constant representing the net magnetic flux contained within the boundary of the solenoidal field coils. This boundary condition is consistent with a perfectly conducting wall, which behaves as a magnetic flux conserver.

The domain extends sufficiently far from the plasma in the z direction so that the magnetic field is purely axial and uniform at the ends. With the pressure function and these boundary conditions, the elliptic Grad–Shafranov equation is solved numerically to provide the axisymmetric solution for $\psi(r,z)$. The magnetic field, $\boldsymbol{B}(r,z)$ is then computed from Eq. (9), and the pressure, $p(r,z)$ is computed from the assumed pressure function, e.g., Eq. (11), and the poloidal flux function, $\psi(r,z)$. In Figs. 1a and 1b, we are showing two sample FRC equilibria; Fig. 1a corresponds to a smaller relative size of the vacuum region compared to the FRC, whereas Fig. 1b corresponds to a larger vacuum region. The streamlines trace the magnetic field, and the contours are pressure. The magnetic flux generated by the plasma current encircles the plasma within the magnetic separatrix. Magnetic field lines are compressed against the flux conserver by the plasma magnetic flux, which produces higher magnetic fields at the midplane.

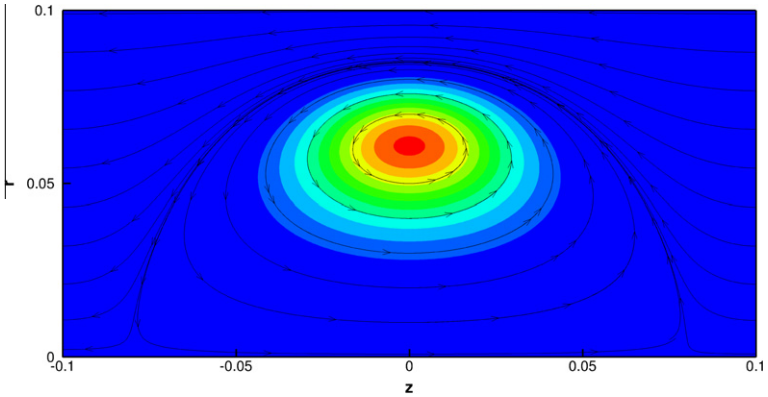

Fig. 1a. Sample FRC equilibrium using the pressure function given in Eq. (11).

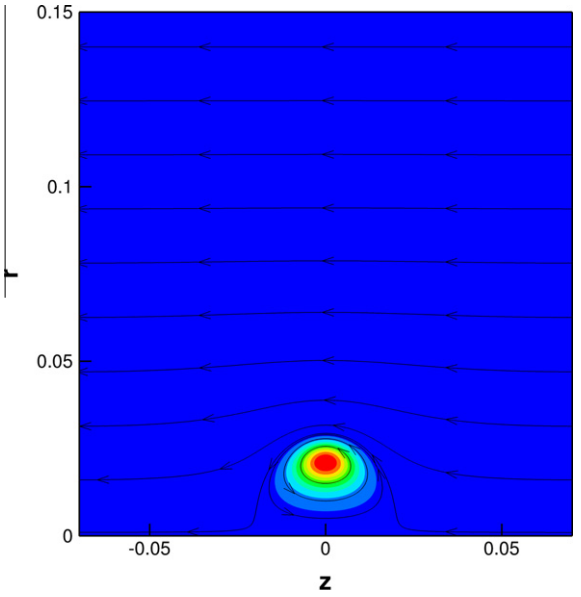

Fig. 1b. Sample FRC equilibrium with a larger vacuum region using the pressure function given in Eq. (11).

1.3. The MACH3 code

The *MACH3* (multiblock arbitrary coordinate hydromagnetic) code, see [3,4], solves the time-dependent, resistive, magnetohydrodynamics (MHD) model in general three-dimensional geometries. The model is described by Eqs. (1), (2), (3), and (7) in addition to an adiabatic equation of state and energy equations for the electron and ion fluids. The code has additional capabilities not relevant to the current investigation.

The *MACH3* code uses an equation splitting algorithm to solve the MHD equations on a non-uniform, three-dimensional mesh that is defined with a block-structured domain. The algorithm splits the equations according to physical effects. For example, Eq. (7) is split into terms associated with advection, Lagrangian dynamics, and magnetic diffusion:

$$\frac{\partial \boldsymbol{B}}{\partial t} = -\underbrace{\boldsymbol{u}\cdot\operatorname{grad}\boldsymbol{B}}_{\text{advection}} + \underbrace{\boldsymbol{B}\cdot\operatorname{grad}\boldsymbol{u} - \boldsymbol{B}\operatorname{div}\boldsymbol{u}}_{\text{Lagrangian dynamics}} + \underbrace{\frac{c^2}{4\pi\sigma}\Delta\boldsymbol{B}}_{\text{diffusion}}, \tag{12}$$

where Eq. (6) has been assumed. The equations of each physical effect are solved self-consistently and coupled with the other model equations using an appropriate numerical algorithm: advection is solved using a second-order upwind method; Lagrangian dynamics are solved using an implicit θ method [5], where $\theta = 1/2$ gives the Crank–Nicolson scheme and $\theta = 1$ gives the backward Euler scheme; and magnetic diffusion is solved with a multigrid method. Boundary conditions are applied after each physical effect is calculated.

The equation splitting algorithm provides an arbitrary Lagrangian–Eulerian (ALE) formulation. In the Lagrangian mode, the mesh moves with the fluid. In the Eulerian mode, the mesh remains in a fixed frame of reference. The ALE formulation allows for any combination of modes, so for example, the mesh can move with the fluid except when grid entanglement occurs.

1.4. Formulation of the problem

Let $D \subset \mathbb{R}^3$ be a bounded domain that contains the FRC plasma. On one hand, this domain should extend beyond the separatrix shown in Figs. 1a and 1b, and on the other hand, it should be completely inside the FRC coils. Specific geometric settings that we use for our simulations are described in Section 3.2. A typical size of the domain D is on the order of decimeters. Inside this domain, the single fluid MHD Eqs. (1), (2), (3), and (7) are integrated by the code *MACH3*, see Section 1.3. However, the magnetic field $\boldsymbol{B}$ due to the plasma currents obviously extends beyond the domain D (theoretically, all the way to infinity, where it vanishes), and hence its accurate numerical simulation requires either solving the governing equations not only on D but on the exterior region (vacuum) as well, or setting an appropriate artificial boundary condition (ABC) for the field at the outer boundary ∂D. Previous computations conducted with the help of *MACH3* adopted the first approach, and the vacuum region was approximated by a very high yet artificial coefficient of magnetic diffusion, see Eq. (7), so that the same equations were solved everywhere. This approach, however, proves intractable for most real problems, because the computational domain appears too large. Indeed, it shall be chosen so that the field due to the plasma currents can be considered negligibly

small at its boundaries.[1] This is true, for example, if the coils are placed sufficiently far away from the FRC, so that the total field at the coils is essentially equal to the field due to the coils only. Then, the entire vacuum region between the FRC and the coils has to be included into the computation. Its size though is much larger than typical diffusion scale lengths, which must be accurately resolved. This leads to excessively large grid dimensions and makes the computations expensive.

An alternative is to truncate the entire vacuum region $\mathbb{R}^3 \setminus D$ and set an ABC for the magnetic field $\boldsymbol{B}$ at the artificial boundary ∂D. The ABC should accurately represent the correct behavior of the solution in the far field, i.e., on the truncated part of the domain. *Developing, setting, and testing of this ABC is the central objective of this paper.* For a general survey of various ABC methodologies we refer the reader to the review publication [6]. To build a good ABC for the current problem, we first need to derive an appropriate model for the field outside D.

This is easy to do by adopting the same assumptions as in Section 1.1. As there is no electric current $\boldsymbol{j}$ in the vacuum, Eq. (3) transforms into $\operatorname{curl}\boldsymbol{B} = \boldsymbol{0}$, which means that there is a scalar magnetic potential $\varphi : \boldsymbol{B} = \operatorname{grad}\varphi$. Then, Eq. (6) implies that this potential satisfies the Laplace equation: $\Delta\varphi = 0$. Finally, applying the operation grad to this equation, we obtain:

$$\Delta\boldsymbol{B} = \boldsymbol{0} \quad \text{on} \quad \mathbb{R}^3 \setminus D. \tag{13}$$

Thus, the magnetic field (due to the plasma currents) outside D satisfies the Laplace equation. Eq. (13) also needs to be supplemented by the condition of vanishing of the field at infinity:

$$\boldsymbol{B} \to \boldsymbol{0} \quad \text{as} \quad |\boldsymbol{x}| \to \infty. \tag{14}$$

The magnetic field $\boldsymbol{B}$ that satisfies Eqs. (13), (14) is quasi-static (rather than truly stationary) because at the boundary ∂D it matches the field that satisfies the evolution Eq. (7) inside D. Note that if the coefficient of magnetic diffusion $\frac{c^2}{4\pi\sigma}$ in Eq. (7) is artificially let go to infinity, then the parabolic Eq. (7) transforms into the elliptic Eq. (13). This explains why earlier simulations with *MACH3* where conducted with an artificially high magnetic diffusion outside D.

Let us additionally note that in practice the magnetic field governed by Eq. (7) or (12) on the domain D shall be interpreted as the total magnetic field, i.e., the sum of the field due to the plasma currents and the field due to the coils. The field due to the coils is incoming with respect to the domain D (because its sources are outside D), it provides the data that drive the problem, and in most cases it can be assumed known explicitly. For the range of formulations that we investigate in the current paper, this field is steady-state, although in general it may vary slowly with time. As the incoming field is known, it can be subtracted from the total field, and then the ABC can be set only for the field due to the plasma currents, i.e., the outgoing field with respect to D. In some situations, one may also need to have the overall field at the boundary ∂D split into the component due to the plasma and the component due to the coils. For example, the split may be desirable to have for the Grad–Shafranov equilibrium described in Section 1.2. As shown in Section 2, the splitting capability is provided by the same apparatus that we use for constructing the ABC.

It is also important to mention that the possibility of a "gradual" transition from Eq. (7) to Eq. (13) as $\sigma \to 0$ indicates that the regularity of the solution will be preserved on the entire $\mathbb{R}^3$ (since the vanishing terms in Eq. (7) are of a lower order compared to $\Delta\boldsymbol{B}$). Hence, the overall solution for the magnetic field $\boldsymbol{B}$, as well as its first normal derivative (flux), shall be assumed continuous across the interface ∂D.[2]

The equation splitting algorithm used in *MACH3*, see formula (12), is well suited for the ABC implementation described here, since only the magnetic field requires setting an ABC (as it extends to infinity). All other variables (i.e., fluid variables) are bounded by the computational domain.

1.5. Outline of the paper

The quasi-static ABC for the magnetic diffusion Eq. (7) based on the exterior model (13), (14) is constructed in Section 2 with the help of Calderon's projection operators [7,8] and the method of difference potentials by Ryaben'kii [9,10]. The method of difference potentials generalizes the original constructs by Calderon and builds a complete discrete analogue of the theory; beyond the pioneering work by Ryaben'kii, its more recent developments can be found, e.g. in [11–14]. In Section 2, we also show how Calderon's boundary projections enable an unambiguous decomposition of the total magnetic field $\boldsymbol{B}$ at the boundary ∂D into the incoming (due to the coils) and outgoing (due to the plasma currents) components. Numerical performance of the ABC built in Section 2 is tested in Section 3. Section 4 summarizes the results and outlines open questions that may merit a further study. In addition, in Appendices A and B we complete the argument toward using the quasi-static ABCs. Specifically, we show that even if we consider genuine wave solutions on $\mathbb{R}^3 \setminus D$, then for those regimes, for which the results of the single fluid MHD inside D stay physical, the frequency dependent ABCs still reduce to the quasi-static ones.

2. Calderon's operators

Eq. (13) is a vector Laplace equation. If, however, the magnetic field $\boldsymbol{B}$ is represented using Cartesian components, then the governing equation for each individual component B will be the standard scalar Laplace equation:

[1] In practice, the computational domain cannot, of course, extend all the way to infinity.

[2] For other physical settings, one can consider alternative, more general, interface conditions at ∂D.

$$\Delta B = 0 \quad \text{on} \quad \mathbb{R}^3 \setminus D \tag{15}$$

that needs to be supplemented by the same condition at infinity as given by (14):

$$B \to 0 \quad \text{as} \quad |\boldsymbol{x}| \to \infty. \tag{16}$$

Hereafter, we will conduct the analysis using the scalar model (15), (16) that applies to each Cartesian component of $\boldsymbol{B}$ independently.

2.1. Continuous Calderon's operators

Let Γ denote the boundary of the computational domain $D, \Gamma = \partial D$, and let

$$G(\boldsymbol{x}) = -\frac{1}{4\pi|\boldsymbol{x}|}$$

be the fundamental solution of the Laplace operator Δ. A generalized potential of Calderon's type, see [9,10], with vector density $\xi_\Gamma = (\xi_0, \xi_1)|_\Gamma$ is defined by the convolution integral:

$$\boldsymbol{P}_D\xi_\Gamma(\boldsymbol{x}) = \int_\Gamma \left(\xi_0(\boldsymbol{y})\frac{\partial G}{\partial \boldsymbol{n}}(\boldsymbol{x}-\boldsymbol{y}) - \xi_1(\boldsymbol{y})G(\boldsymbol{x}-\boldsymbol{y})\right)ds_{\boldsymbol{y}}, \quad \boldsymbol{x} \in \mathbb{R}^3 \setminus D. \tag{17}$$

For any (sufficiently smooth) function v specified on $\mathbb{R}^3 \setminus D$ we also introduce its vector trace on Γ:

$$\boldsymbol{Tr}\, v \stackrel{\text{def}}{=} \left(v, \frac{\partial v}{\partial \boldsymbol{n}}\right)\Big|_\Gamma. \tag{18}$$

If the density ξ_Γ happens to be the trace (18) of a solution $B(\boldsymbol{x}), \boldsymbol{x} \in \mathbb{R}^3 \setminus D$, that satisfies (16), then the potential $\boldsymbol{P}_D\xi_\Gamma(\boldsymbol{x})$ of (17) coincides with $B(\boldsymbol{x})$ and Eq. (17) becomes the classical Green's formula [15]. The Calderon projection biP_Γ is defined as the trace (18) of the potential biP_D of (17):

$$\boldsymbol{P}_\Gamma\xi_\Gamma \stackrel{\text{def}}{=} \boldsymbol{Tr}\boldsymbol{P}_D\xi_\Gamma. \tag{19}$$

It is easy to make sure that $\boldsymbol{P}_\Gamma^2 = \boldsymbol{P}_\Gamma$. Indeed, $\forall\ \xi_\Gamma : \Delta\boldsymbol{P}_D\xi_\Gamma = 0, \boldsymbol{x} \in \mathbb{R}^3 \setminus D$. Then, applying the Green's formula $v = \boldsymbol{P}_D\boldsymbol{Tr}\, v$, where $\boldsymbol{Tr}$ is defined by (18), to $v = \boldsymbol{P}_D\xi_\Gamma$, we have: $\boldsymbol{P}_D\xi_\Gamma = \boldsymbol{P}_D\boldsymbol{Tr}\boldsymbol{P}_D\xi_\Gamma$. Using the operator $\boldsymbol{Tr}$ on both sides of this equality, one immediately gets $biP_\Gamma^2 = biP_\Gamma$.

The key property [9–11] of the operator biP_Γ of (19) is that *those and only those ξ_Γ that satisfy the boundary equation with projection (BEP):*

$$\boldsymbol{P}_\Gamma\xi_\Gamma = \xi_\Gamma \tag{20}$$

are traces (18) of the solution $B(\boldsymbol{x})$ to (15), (16): $\xi_\Gamma = \boldsymbol{Tr}B$. Indeed, let $B(\boldsymbol{x})$ be harmonic on $\mathbb{R}^3 \setminus D, \Delta B = 0$, and $B \to 0$ as $|\boldsymbol{x}| \to \infty$. Then, the Green's formula yields $B = \boldsymbol{P}_D\boldsymbol{Tr}B$, and applying the operator $\boldsymbol{Tr}$ of (18), we arrive at (20). Conversely, let the BEP (20) hold for some ξ_Γ. Denote $B = \boldsymbol{P}_D\xi_\Gamma$; clearly, $\Delta B = 0$ on $\mathbb{R}^3 \setminus D$. Moreover, equality (20) implies that $\boldsymbol{Tr}B = \xi_\Gamma$.

Altogether, we see that the BEP (20) equivalently replaces the Laplace Eq. (15) along with the condition (16) on the exterior region $\mathbb{R}^3 \setminus D$, and hence provides an ideal exact ABC for the magnetic diffusion Eq. (7) solved on D. This ABC is *nonlocal* as it relates the values of the solution B and its first normal derivative $\frac{\partial B}{\partial \boldsymbol{n}}$ along the entire artificial boundary Γ.

Note that the field $B(\boldsymbol{x})$ that satisfies (15), (16) does not have any sources (currents that drive it) on $\mathbb{R}^3 \setminus D$, and hence shall be interpreted as outgoing with respect to the domain D (all its sources are the plasma currents inside D). Consequently, a given ξ_Γ can be the trace of an outgoing field if and only if it satisfies the BEP (20) or equivalently, if and only if it belongs to the range of the Calderon projection $\boldsymbol{P}_\Gamma$ of (19): $\xi_\Gamma \in \mathrm{Im}\boldsymbol{P}_\Gamma$. As such, the Calderon projection $\boldsymbol{P}_\Gamma$ unambiguously partitions an arbitrary ξ_Γ into two components: $\xi_\Gamma = \xi_\Gamma^{(\mathrm{out})} + \xi_\Gamma^{(\mathrm{inc})}$, where $\xi_\Gamma^{(\mathrm{out})} = \boldsymbol{P}_\Gamma\xi_\Gamma \in \mathrm{Im}\boldsymbol{P}_\Gamma$ is the outgoing part that belongs to the range of the projection (because $\boldsymbol{P}_\Gamma^2 = \boldsymbol{P}_\Gamma$), and $\xi_\Gamma^{(\mathrm{inc})} = \xi_\Gamma - \xi_\Gamma^{(\mathrm{out})} \in \mathrm{Ker}\boldsymbol{P}_\Gamma$ is the incoming part that belongs to the kernel (null space) of the projection. Accordingly, the entire space of traces ξ_Γ on the boundary $\Gamma = \partial D$ can be represented as a direct sum of the subspaces of outgoing and incoming fields, $\mathrm{Im}\boldsymbol{P}_\Gamma \oplus \mathrm{Ker}\boldsymbol{P}_\Gamma$, i.e., the fields due to the sources inside and outside D, respectively.

Let now $\xi_\Gamma = (\xi_0, \xi_1)$ be given, and take an arbitrary (sufficiently smooth) function $w(\boldsymbol{x}), \boldsymbol{x} \in \mathbb{R}^3$, that has the trace $\xi_\Gamma : \boldsymbol{Tr}w = \xi_\Gamma$, and satisfies the condition at infinity (16). Since generally speaking $\Delta w \neq 0, \boldsymbol{x} \in \mathbb{R}^3 \setminus D$, the Green's formula for w becomes:

$$w(\boldsymbol{x}) = \int_{\mathbb{R}^3\setminus D} G\Delta w d\boldsymbol{y} + \int_\Gamma \left(w\frac{\partial G}{\partial \boldsymbol{n}} - \frac{\partial w}{\partial \boldsymbol{n}}G\right)ds_{\boldsymbol{y}}, \quad \boldsymbol{x} \in \mathbb{R}^3 \setminus D.$$

Hence, the Calderon potential (17) can be equivalently re-defined as follows:

$$\boldsymbol{P}_D\xi_\Gamma(\boldsymbol{x}) = w(\boldsymbol{x}) - \int_{\mathbb{R}^3\setminus D} G\Delta w d\boldsymbol{y} \equiv \int_D G\Delta w d\boldsymbol{y}, \quad \boldsymbol{x} \in \mathbb{R}^3 \setminus D. \tag{21}$$

The potential (21) is insensitive to the choice of w as long as $\boldsymbol{Tr}w = \xi_\Gamma$. The projection $\boldsymbol{P}_\Gamma$ defined by (21), (19) is the same as (17), (19). The importance of the new definition (21) is that it does not contain surface integrals and enables efficient implementation for finite differences using volumetric convolution with the discrete fundamental solution, see Section 2.2 and Appendix C. In doing so, the correct far-field behavior of the solution is accounted for automatically by the structure of the discrete fundamental solution, see Appendix C. Moreover, this approach also leads to an efficient coupling with the *MACH3* code that employs a finite volume discretization.

Formula (21) is important from another standpoint as well. The integral on the right-hand side of the last equality in (21) is a solution to the Poisson equation on $\mathbb{R}^3$:

$$\Delta u = g_D, \tag{22}$$

subject to the condition at infinity (16). The right-hand side $g_D \stackrel{\text{def}}{=} \Delta w|_D$ of Eq. (22) is compactly supported on $\mathbb{R}^3$ (w is given). This Poisson problem is referred to as *the auxiliary problem (AP)*, see [10]. It does not, in fact, have to be solved on the entire $\mathbb{R}^3$. Instead, it can be solved on a regular bounded domain that contains D, such as a larger ball, for which the exact ABC at the outer boundary (a sphere) can be obtained by the separation of variables, see Appendix B. This approach allows us to extend the argument made in Appendix B.3 (on the convergence of frequency dependent ABCs to quasi-static ABCs as the wavelength increases) from the spherical artificial boundary to the artificial boundary ∂D of a more general shape, see Appendix B.4.

Moreover, while in this paper we are solving the AP with the help of a discrete volumetric convolution, using an equivalent formulation, e.g., the one that involves a larger auxiliary domain (a larger ball) and choosing an alternative solution strategy, e.g., the separation of variables, may be very useful for a number of applications beyond those addressed hereafter, see [6,10].

2.2. Discrete Calderon's operators

The theory and numerical implementation of discrete Calderon's operators constitute the essence of the method of difference potentials [10]. For implementation in the current paper, we are using a Cartesian grid on the space $\mathbb{R}^3$. Let us denote this grid by $\mathbb{N}$, and let us assume for simplicity that the grid size h is the same in all three coordinate directions. The latter assumption can be alleviated and does not present any loss of generality. The Laplace Eq. (15) is approximated on the grid $\mathbb{N}$ with second order accuracy using central differences:

$$\Delta^{(h)}B \equiv \frac{B_{i+1,j,k} - 2B_{i,j,k} + B_{i-1,j,k}}{h^2} + \frac{B_{i,j+1,k} - 2B_{i,j,k} + B_{i,j-1,k}}{h^2} + \frac{B_{i,j,k+1} - 2B_{i,j,k} + B_{i,j,k-1}}{h^2} = 0. \tag{23}$$

We choose the computational domain D to be a parallelepiped aligned with the grid. In general, this geometric limitation may be lifted, but in the meantime it provides a straightforward venue toward conducting the numerical experiments, see Section 3. We note however that the type of limitation the rectangular shape of D presents is not the same as those often encountered in the literature when constructing the exact nonlocal ABCs, such as DtN maps [6]. Indeed, the most common geometric limitations originate from the requirement that ∂D be a "separable" surface, i.e., a coordinate surface in the system of coordinates that would allow the separation of variables in the governing equations. The surface of a parallelepiped is not separable though, and is chosen primarily for the convenience of coupling the ABCs with *MACH3* rather than for the convenience of computing the ABCs themselves. In general, the computation of Calderon's operators and ABCs does not require that the boundary ∂D be separable, or that it should conform to the grid lines. If, however, the shape of the boundary is most general, and the interior grid on D is not the same as the grid on which the Calderon operators are computed (Cartesian grid $\mathbb{N}$ hereafter), then the construction of the ABCs may require additional steps, such as interpolation between the grids, see, e.g. [16]. Those are precisely the steps that we are trying to avoid in the current paper.

Note also that the boundary ∂D we have chosen it is not smooth either because it has edges and vertices. A harmonic function on $\mathbb{R}^3 \setminus D$ may have singularities (unbounded derivatives) at those edges and vertices. We, however, are interested in sufficiently smooth solutions that vanish at infinity and are bounded along with their derivatives all the way up to the interface, i.e., in those solutions that can be thought of as smooth extensions from D to $\mathbb{R}^3 \setminus D$.

To accurately define the approximation, we will need to introduce another grid $\mathbb{M}$ along with the previously defined $\mathbb{N}$. On the grid $\mathbb{M}$, we will consider the residuals of the operator $\Delta^{(h)}$ of (23). For our particular case, the individual nodes $n = (i,j,k)$ and $m = (i,j,k)$ of the grids $\mathbb{N}$ and $\mathbb{M}$ coincide,[3] but we need to make a distinction between $\mathbb{N}$ and $\mathbb{M}$ to tell between the solutions and the right-hand sides of the inhomogeneous finite-difference equations. We also denote by $\mathbb{N}_m$ the stencil of the discrete Laplacian $\Delta^{(h)}$ centered at a given $m \in \mathbb{M}$. For the approximation that we have chosen, this stencil is symmetric and contains seven grid nodes altogether, see formula (23). Note that other approximations (schemes) and other stencils can be used as well, see [10].

Next, we denote $D_1 = \mathbb{R}^3 \setminus \bar{D}$ ($\bar{D}$ is the set theoretical closure of D) and introduce the following subsets of the grids $\mathbb{M}$ and $\mathbb{N}$, which will allow us to clearly distinguish between the interior and exterior domains, interior and exterior sources, and interior and exterior solutions:

[3] It does not have to be the case in general, see [10].

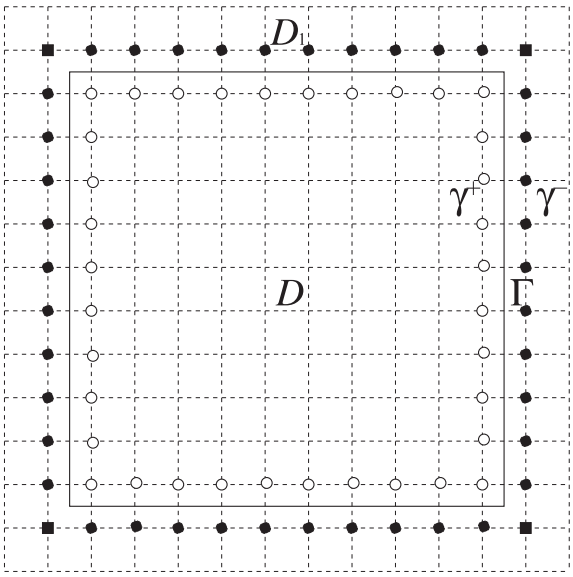

Fig. 2. 2D schematic: γ^+ — hollow bullets, γ^- — filled bullets, corner nodes — filled boxes.

$$\begin{aligned}
&\mathbb{M}^+ = \mathbb{M} \cap \bar{D}, \quad \mathbb{M}^- = \mathbb{M} \setminus \mathbb{M}^+ = \mathbb{M} \cap D_1, \\
&\mathbb{N}^+ = \cup_{m\in\mathbb{M}^+} \mathbb{N}_m, \quad \mathbb{N}^- = \cup_{m\in\mathbb{M}^-} \mathbb{N}_m, \\
&\gamma = \mathbb{N}^+ \cap \mathbb{N}^-, \quad \gamma^+ = \mathbb{N}^- \cap D, \quad \gamma^- = \mathbb{N}^+ \cap D_1.
\end{aligned} \tag{24}$$

We emphasize that the grid $\mathbb{M}$ that pertains to the residuals of the finite-difference operator $\Delta^{(h)}$ is partitioned into $\mathbb{M}^+$ and $\mathbb{M}^-$ directly, i.e., following the geometry of D and D_1. In contradistinction to that, the grid $\mathbb{N}$ is not partitioned directly; we rather consider the collection of all nodes of $\mathbb{N}$ swept by the stencil $\mathbb{N}_m$ when its center belongs to $\mathbb{M}^+$, and call this subgrid $\mathbb{N}^+$; see (24). Obviously, some of the nodes of $\mathbb{N}^+$ obtained by this approach happen to be outside D, i.e., in D_1, and these nodes are called γ^-. The sets $\mathbb{N}^-$ and γ^+ are defined similarly starting from $\mathbb{M}^-$. The key idea is that whereas the grids $\mathbb{M}^+$ and $\mathbb{M}^-$ do not overlap, the grids $\mathbb{N}^+$ and $\mathbb{N}^-$ do overlap, and their overlap is denoted γ; obviously, $\gamma = \gamma^+ \cup \gamma^-$. The subset of grid nodes γ is called *the grid boundary*; it is a fringe of nodes that is located near the continuous boundary Γ and in some sense straddles it. The specific structure of γ obviously depends on the construction of the operator $\Delta^{(h)}$ and the stencil $\mathbb{N}_m$. In Fig. 2, we are schematically showing the grid boundary γ and its subsets γ^+ and γ^- for the two-dimensional central difference second order Laplacian similar to that introduced in Eq. (23) for the three-dimensional case. It is a two-layer fringe of grid nodes located near the continuous boundary Γ.

We also note that the 7-point central difference stencil of the Laplacian $\Delta^{(h)}$ of (23), as well as its 5-point two-dimensional counterpart, are such that the exterior corner nodes do not belong to γ, see (24). Those nodes are shown by filled boxes in Fig. 2 in the two-dimensional case, and in 3D there are two types of corner nodes — edges and vertices. It is, however, explained below that from the standpoint of setting the ABCs those corner nodes may become important.

The idea of setting the ABCs for a discretization is as follows. Assume that the magnetic diffusion Eq. (7) is approximated on D (with second order accuracy) using the same grid $\mathbb{N}$ and the same stencil $\mathbb{N}_m$ in space. Then, the nodes γ^- shall be interpreted as ghost nodes for this discretization. In other words, if the solution is known on $\mathbb{N}^+ \setminus \gamma^-$, i.e., strictly inside D, then its values at the ghost nodes γ^- (i.e., on the rest of $\mathbb{N}^+$) shall be provided so that the finite difference approximation of (7) can be obtained for every node of $\mathbb{M}^+$. Specifying those ghost values means building a closure for the interior scheme. Of course, if we knew how to actually solve the extended problem that includes the discrete Laplace equation (23) outside D, then we would have immediately obtained the required closure. The direct solution, however, is not possible because the domain D_1 is unbounded. Hence, the ghost values must be obtained using an alternative strategy that would still be equivalent though to having the discretized Laplace equation solved on the exterior region. This alternative strategy will be based on the discrete Calderon operators.

In a somewhat more general setting that we adopt in the current paper, the discretization inside D does not have to be built on the same stencil $\mathbb{N}_m$, although the grid is assumed the same.[4] Specifically, we use the standard 7-node central difference Laplacian (23) to discretize the governing equation in the far field, whereas the code *MACH3* that we use for computations inside D and all the way up to its boundary ∂D is built on the full $3 \times 3 \times 3 = 27$-node stencil. In this case, the set of ghost nodes

[4] Interior grid is assumed to be the same as the exterior grid at least near the boundary Γ. In an even more general setting, the grid inside D does not have to be the same as the one outside D, see, e.g., [16,6].

appears larger than γ^-. As the stencil of *MACH3* involves the edge centers and the vertices, then the corner nodes, see Fig. 2, are included[5]:

$$\tilde{\gamma}^- \equiv \{\text{ghost nodes}\} = \gamma^- \cup \{\text{corner nodes}\}. \tag{25}$$

The discrete Calderon operators that we will use for constructing the ABCs are Calderon's potentials and Calderon's boundary projections. Let ξ_γ be a grid function defined on the grid boundary γ, see formula (24). This ξ_γ will be called the density of the potential. A discrete Calderon's potential takes ξ_γ as its argument and produces a grid function on the entire grid $\mathbb{N}^-$. As $\mathbb{N}^-$ is unbounded, in practice the potential needs to be evaluated only on some finite subset of nodes of the grid $\mathbb{N}^-$, specifically, at the ghost nodes $\tilde{\gamma}^-$, see formula (25). A discrete Calderon's projection takes ξ_γ as its argument and produces another grid function defined on γ. The key property of Calderon's projections which, in particular, makes them so well suited for setting the ABCs, is that the projection of ξ_γ coincides with ξ_γ itself if and only if this ξ_γ is the trace on γ of a solution to the discrete Laplace Eq. (23) defined on the entire $\mathbb{N}^-$.

For a given density of the potential ξ_γ, the discrete Calderon operators are defined as follows. First, the density is extended from γ to $\mathbb{N}$ by zero:

$$w_{\mathbb{N}} = \begin{cases} \xi_\gamma & \text{on} \quad \gamma, \\ 0 & \text{on} \quad \mathbb{N} \setminus \gamma. \end{cases} \tag{26}$$

Then, the discrete Laplacian $\Delta^{(h)}$ is applied, and the result is truncated to $\mathbb{M}^+$:

$$g_{\mathbb{M}} = \begin{cases} \Delta^{(h)} w_{\mathbb{N}} & \text{on} \quad \mathbb{M}^+, \\ 0 & \text{on} \quad \mathbb{M}^-. \end{cases} \tag{27}$$

The function $g_{\mathbb{M}}$ of (27) is used as the right-hand side (RHS) of the discrete Poisson equation to be solved on the grid $\mathbb{N}$ (cf. formula (22)):

$$\Delta^{(h)} u_{\mathbb{N}} = g_{\mathbb{M}}. \tag{28}$$

It is required that the solution to Eq. (28) vanish at infinity (in 3D). The solution $u_{\mathbb{N}}$ to this equation considered only on the exterior region or, more precisely, on the grid $\mathbb{N}^-$, is called *the discrete Calderon potential (or difference potential, see [10]) with the density* ξ_γ (cf. formula (21)):

$$\boldsymbol{P}_{\mathbb{N}^-\gamma} \xi_\gamma = u_{\mathbb{N}}|_{\mathbb{N}^-}. \tag{29}$$

As the RHS of Eq. (28) is compactly supported on $\mathbb{M}^+$, see formula (27), it is clear that the potential $\boldsymbol{P}_{\mathbb{N}^-\gamma}\xi_\gamma$ of (29) solves the discrete Laplace equation:

$$\Delta^{(h)} \left(\boldsymbol{P}_{\mathbb{N}^-\gamma} \xi_\gamma \right) = 0 \quad \text{on} \quad \mathbb{M}^-. \tag{30}$$

The trace of the potential $\boldsymbol{P}_{\mathbb{N}^-\gamma}\xi_\gamma$ of (29) on the grid boundary γ is called *the discrete Calderon boundary projection* (cf. formula (19)):

$$\boldsymbol{P}_\gamma \xi_\gamma \stackrel{\text{def}}{=} \left(\boldsymbol{P}_{\mathbb{N}^-\gamma} \xi_\gamma \right)|_\gamma. \tag{31}$$

To show that $\boldsymbol{P}_\gamma^2 = \boldsymbol{P}_\gamma$, take an arbitrary ξ_γ and denote $v_{\mathbb{N}^-} = \boldsymbol{P}_{\mathbb{N}^-\gamma}\xi_\gamma$; clearly, $\Delta^{(h)} v_{\mathbb{N}^-} = 0$ on $\mathbb{M}^-$ because of (30). Let $v_{\mathbb{N}} = v_{\mathbb{N}^-}$ on $\mathbb{N}^-$ and $v_{\mathbb{N}} = 0$ on $\mathbb{N} \setminus \mathbb{N}^-$. Denote $f_{\mathbb{M}} = \Delta^{(h)} v_{\mathbb{N}}$; obviously, $v_{\mathbb{N}}$ coincides with the solution $u_{\mathbb{N}}$ of the discrete Poisson equation $\Delta^{(h)} u_{\mathbb{N}} = f_{\mathbb{M}}$ that vanishes at infinity. On the other hand, $f_{\mathbb{M}} = 0$ on $\mathbb{M}^-$ because $\Delta^{(h)} v_{\mathbb{N}} = \Delta^{(h)} v_{\mathbb{N}^-} = 0$ on $\mathbb{M}^-$. Consequently, $f_{\mathbb{M}}$ coincides with $g_{\mathbb{M}}$ of (27) if the latter is defined via $w_{\mathbb{N}} = v_{\mathbb{N}^-}|_\gamma$ on γ and $w_{\mathbb{N}} = 0$ on $N \setminus \gamma$ (cf. formula (26)). Therefore, $v_{\mathbb{N}}$ is a solution to $\Delta^{(h)} v_{\mathbb{N}} = g_{\mathbb{M}}$ (vanishing at infinity), and hence $v_{\mathbb{N}^-} = \boldsymbol{P}_{\mathbb{N}^-\gamma}\left(v_{\mathbb{N}^-}|_\gamma \right)$, which is a discrete analogue of the classical Green's formula. Taking the trace of the last equality on γ and recalling that $v_{\mathbb{N}^-}|_\gamma = \boldsymbol{P}_\gamma \xi_\gamma$ because of (31), we obtain $\boldsymbol{P}_\gamma \xi_\gamma = \boldsymbol{P}_\gamma^2 \xi_\gamma$.

The most important property of the discrete Calderon's projection $\boldsymbol{P}_\gamma$ of (31) is that a given density ξ_γ appears to be the trace on γ of a solution $v_{\mathbb{N}^-}$ to the discrete Laplace equation if and only if ξ_γ satisfies *the discrete boundary equation with projection (BEP)* (cf. formula (20)):

$$\boldsymbol{P}_\gamma \xi_\gamma = \xi_\gamma. \tag{32}$$

In other words, the discrete BEP (32) holds if and only if there exists $v_{\mathbb{N}^-}$ that vanishes at infinity and such that

$$\Delta^{(h)} v_{\mathbb{N}^-} = 0 \quad \text{on} \quad \mathbb{M}^- \,\&\, v_{\mathbb{N}^-}|_\gamma = \xi_\gamma. \tag{33}$$

[5] There are only four corner nodes in the 2D setting shown in Fig. 2, but in 3D the corner nodes include both edges and vertices of the cubic computational domain.

To prove the aforementioned equivalence, we first notice that if the BEP (32) holds, then the function $v_{\mathbb{N}^-}$ that satisfies (33) is the Calderon potential with the density ξ_γ: $v_{\mathbb{N}^-} = \boldsymbol{P}_{\mathbb{N}^-\gamma}\xi_\gamma$. Indeed, the first condition of (33) follows from (30), while the second one is an implication of the BEP (32) itself. Conversely, let $v_{\mathbb{N}^-}$ satisfy the equation $\Delta^{(h)} v_{\mathbb{N}^-} = 0$ on $\mathbb{M}^-$ and vanish at infinity. Then, as we have seen, $v_{\mathbb{N}^-}$ can be represented by the discrete Green's formula: $v_{\mathbb{N}^-} = \boldsymbol{P}_{\mathbb{N}^-\gamma}\left(v_{\mathbb{N}^-}|_\gamma\right)$. Taking the trace of this equality on γ and denoting $\xi_\gamma = v_{\mathbb{N}^-}|_\gamma$, we obtain (32).

The equivalence of (32) and (33) makes the BEP (32) an ideal ABC for the interior scheme. Indeed, by definition the BEP (32) connects only the values of the solution on the grid boundary γ. In other words, it can be thought of as providing a relation between the ghost values on γ^- and the interior boundary values on γ^+. By construction, this relation is equivalent to having the discrete Laplace equation solved on the grid $\mathbb{N}^-$. Therefore, it provides a closure (separately for each Cartesian component of $\boldsymbol{B}$) for the discrete counterpart of Eq. (7) on $\mathbb{N}^+$, which would be equivalent to solving the combined problem (7), (13), (14) on the entire grid $\mathbb{N}$.

Similarly to the continuous case, see Section 2.1, the discrete boundary projection $\boldsymbol{P}_\gamma$ of (31) enables a partition of the entire space of grid functions ξ_γ into the direct sum of two subspaces: $\mathrm{Im}\boldsymbol{P}_\gamma \oplus \mathrm{Ker}\boldsymbol{P}_\gamma$. The range of the projection $\mathrm{Im}\boldsymbol{P}_\gamma$ contains traces of the outgoing fields, i.e., the fields with the sources inside D, whereas the kernel of the projection $\mathrm{Ker}\boldsymbol{P}_\gamma$ contains traces of the incoming fields, i.e., the fields with the sources outside D. Equivalently, an arbitrary grid function ξ_γ is represented as the sum of two components:

$$\xi_\gamma = \boldsymbol{P}_\gamma\xi_\gamma + (\boldsymbol{I} - \boldsymbol{P}_\gamma)\xi_\gamma \stackrel{\mathrm{def}}{=} \xi_\gamma^{(\mathrm{out})} + \xi_\gamma^{(\mathrm{inc})}, \tag{34}$$

where $\xi_\gamma^{(\mathrm{out})} = \boldsymbol{P}_\gamma\xi_\gamma \in \mathrm{Im}\boldsymbol{P}_\gamma$ and t $\xi_\gamma^{(\mathrm{inc})} = \xi_\gamma - \xi_\gamma^{(\mathrm{out})} \in \mathrm{Ker}\boldsymbol{P}_\gamma$.

The key practical question is how to compute the discrete Calderon potential and projection for a given density ξ_γ or, in other words, how to solve the Poisson Eq. (28) on the grid $\mathbb{N}$ subject to the condition of having the solution vanish at infinity. This part of the algorithm is often referred to as the discrete auxiliary problem. The discrete AP is solved by *convolution with the fundamental solution $G^{(h)}$ of the discrete Laplace operator:*

$$u_{\mathbb{N}}(n) = \sum_{m\in\mathbb{M}^+} G^{(h)}(n-m)g_{\mathbb{M}}(m). \tag{35}$$

The concept of the discrete fundamental solution $G^{(h)}$ is outlined in Appendix C. It is shown, in particular, that solution (35) vanishes at infinity (see also an equivalent formula (82)).

2.3. Artificial boundary conditions

Actual implementation of the ABC obtained in the form of a discrete BEP (32) depends on how the interior problem is solved on D. If, for example, the magnetic diffusion Eq. (7) is integrated implicitly in time, than relation (32) can be added to the overall system solved on the upper time level. In the case of explicit time marching, it may be convenient to use a resolved form of the BEP (32), i.e., to express the ghost values on γ^- through the interior boundary values on γ^+. To solve Eq. (32) with respect to ξ_{γ^-} for a given ξ_{γ^+}, we first partition the matrix of the operator $\boldsymbol{P}_\gamma$ as schematically shown in Fig. 3. Then, Eq. (32) can be recast as follows:

$$\begin{bmatrix} \boldsymbol{P}_{\gamma^-\gamma^+} \\ \boldsymbol{P}_{\gamma^-\gamma^-} - \boldsymbol{I} \end{bmatrix} \xi_{\gamma^-} = -\begin{bmatrix} \boldsymbol{P}_{\gamma^+\gamma^+} - \boldsymbol{I} \\ \boldsymbol{P}_{\gamma^+\gamma^-} \end{bmatrix} \xi_{\gamma^+}, \tag{36}$$

where $\boldsymbol{I}$ denotes identity matrix of the corresponding dimension in every instance. The following sub-system of (36) can be solved in the classical sense with respect to ξ_{γ^-}:

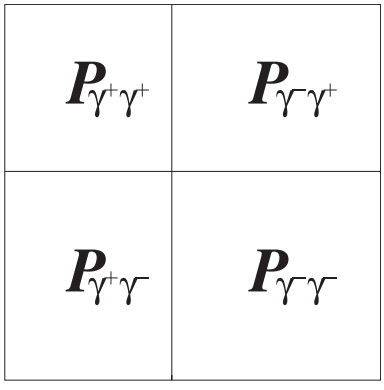

Fig. 3. Partitioning of the discrete Calderon projection $\boldsymbol{P}_\gamma$.

$$(\boldsymbol{P}_{\gamma^-\gamma^-} - \boldsymbol{I})\xi_{\gamma^-} = -\boldsymbol{P}_{\gamma^+\gamma^-}\xi_{\gamma^+}. \tag{37}$$

This way, we obtain the ABC in the form:

$$\xi_{\gamma^-} = -(\boldsymbol{P}_{\gamma^-\gamma^-} - \boldsymbol{I})^{-1}\boldsymbol{P}_{\gamma^+\gamma^-}\xi_{\gamma^+} \stackrel{\text{def}}{=} \boldsymbol{T}\xi_{\gamma^+}. \tag{38}$$

Alternatively, the full system (36) can be solved in the sense of the least squares. This approach may provide additional robustness, whereas solving system (37) in the classical sense is more economical.

The ABC (38) is almost what we want to have, except that it does not specify the corner nodes, see Fig. 2, and hence does not define all the required ghost values, see formula (25). To obtain the missing corners for a given ξ_{γ^+}, we first apply (38) and define the new density of the potential:

$$\xi_\gamma = \begin{bmatrix} \xi_{\gamma^+} \\ \boldsymbol{T}\xi_{\gamma^+} \end{bmatrix} = \begin{bmatrix} \boldsymbol{I} \\ \boldsymbol{T} \end{bmatrix} \xi_{\gamma^+}. \tag{39}$$

Then, we compute the potential (29) with the density ξ_γ of (39) and evaluate it at the corner nodes, i.e., at the edges and vertices in 3D:

$$\xi_{\text{corners}} = \boldsymbol{P}_{\mathbb{N}^-\gamma}\xi_\gamma|_{\text{corners}} = \boldsymbol{P}_{\mathbb{N}^-\gamma}\begin{bmatrix} \boldsymbol{I} \\ \boldsymbol{T} \end{bmatrix} \xi_{\gamma^+}|_{\text{corners}}. \tag{40}$$

Combining (38) and (40), we obtain the full ABC:

$$\xi_{\tilde{\gamma}^-} = \tilde{\boldsymbol{T}}\xi_{\gamma^+}, \tag{41}$$

where $\tilde{\gamma}^-$ is defined by formula (25). Similarly to the continuous case, the ABC (41) is nonlocal, i.e., it couples the values of the solution along the entire external artificial boundary. In general, the ABCs that provide high accuracy and minimize or completely eliminate the error associated with the domain truncation (such as the ABC (41)) often appear nonlocal, see [6].

2.4. Implementation details

As indicated in Section 1.4, in practice the magnetic field $\boldsymbol{B}$ governed by Eq. (7) contains both the outgoing and the incoming components with respect to the domain D, i.e., the component due to the plasma currents and that due to the external coils, respectively. The boundary condition (41), however, applies only to the outgoing component. Hence, the implementation of the boundary condition (41) shall be done in three steps:

1. Subtract the external (incoming) field from the total field at $\gamma^+ : \boldsymbol{B}^{(\text{out})}_{\gamma^+} = \boldsymbol{B}_{\gamma^+} - \boldsymbol{B}^{(\text{inc})}_{\gamma^+}$.
2. Obtain the ghost values of the outgoing field $\boldsymbol{B}^{(\text{out})}_{\tilde{\gamma}^-}$ with the help of (41).
3. Restore the values of the total field on the entire grid boundary $\gamma : \boldsymbol{B}_\gamma = \boldsymbol{B}^{(\text{out})}_\gamma + \boldsymbol{B}^{(\text{inc})}_\gamma$.

In doing so, it is assumed that the external (incoming) field $\boldsymbol{B}^{(\text{inc})}$, which provides the data for the problem, is known. For example, if the electric currents in the coils are given, then the field $\boldsymbol{B}^{(\text{inc})}$ at any location can be computed using the Biot–Savart law. If the simulation starts from an equilibrium solution of the Grad–Shafranov type (Section 1.2), then the initial partition of the total field at the boundary γ into the incoming and outgoing components can be rendered by applying the Calderon projection $\boldsymbol{P}_\gamma$ itself, see formula (34). Subsequently the increment of the time-dependent external field is subtracted prior to the application of formula (41). Specific implementation setting, including domain sizes, grid dimensions, etc., are described in Section 3.

As described in Section 1.2, the FRC equilibrium is surrounded by solenoidal field coils that constrain the net magnetic flux ψ_{net} to a constant value within the cylindrical boundary. The magnetic field $\boldsymbol{B}^{(\text{inc})}$ can then be computed for any equilibrium enclosed within a flux conserver by integrating the magnetic flux through an axial surface as

$$B_z^{(\text{inc})} = \frac{\psi_{net}}{\pi r_w^2} = \frac{1}{\pi r_w^2}\int_0^{r_w} 2\pi r \boldsymbol{B}\cdot\hat{z}\,dr, \tag{42}$$

where $\boldsymbol{B}$ is the total magnetic field of the FRC, which is poloidal,[6] r_w is the radius of the flux conserver, r is the radial coordinate, and $\hat{z}$ is the unit vector in the axial direction in a cylindrical coordinate system. Since ψ_{net} is independent of axial position, Eq. (42) can be evaluated at any position, and $B_z^{(\text{inc})}$ is constant along the cylindrical boundary and corresponds to the magnetic field from the solenoidal field coils. The incoming field is then $\boldsymbol{B}^{(\text{inc})} = B_z^{(\text{inc})}\hat{z}$. The magnetic field $\boldsymbol{B}^{(\text{out})}$ contains the entire contribution to the total magnetic field from the plasma currents.

The ABC (41) needs to be applied on every step of the time marching algorithm for Eq. (7). Hence, it is convenient to precompute the operator $\tilde{\boldsymbol{T}}$ in the form of a matrix, and then apply the ABC via a straightforward matrix–vector multiplication. Computation of the matrix $\tilde{\boldsymbol{T}}$ first requires computing the blocks $\boldsymbol{P}_{\gamma^-\gamma^-}$ and $\boldsymbol{P}_{\gamma^+\gamma^-}$ of the Calderon projection $\boldsymbol{P}_\gamma$, see Fig. 3. This

[6] See, e.g. [17, page 666] for the definition of toroidal coordinates.

is done column by column. In the space of vectors ξ_γ (the dimension of this space is equal to the number of nodes $|\gamma|$ in the grid boundary γ) we choose a basis of vectors that each has only one non-zero component equal to one and all other components equal to zero:

$$\xi_i = [\underbrace{0\ldots010\ldots0}_{i\text{th component}=1}]^T, \quad i = 1,2,\ldots,|\gamma|. \tag{43}$$

Then, individual columns of the matrix $\boldsymbol{P}_\gamma$ correspond to individual basis vectors ξ_i of (43); they are obtained by taking each ξ_i as ξ_γ and performing the computations according to formulae (26)–(31). Inversion of the matrix $\boldsymbol{P}_{\gamma^-\gamma^-} - \boldsymbol{I}$ in formula (58) is done by the LU decomposition. From the standpoint of complexity, it proves acceptable for moderate dimensions; for higher dimensions an iterative solver may need to be employed.

Once the matrix $\boldsymbol{T}$ of (38) is built, we still need to compute the corners and obtain the matrix $\tilde{\boldsymbol{T}}$ of the full ABC (41). This is done using the same basis (43) or, more precisely, its sub-basis that corresponds to γ^+. Namely, we consider all the basis vectors ξ_i of (43), for which the non-zero component corresponds to a node from γ^+. For each of those vectors, we compute the corresponding ξ_{γ^-} and thus arrive at ξ_γ according to (39). Then, we use formula (40) to evaluate the missing corners using the Calderon potential. When this procedure is complete, we obtain the additional rows of the matrix that correspond to the corner nodes, and by adding those rows to $\boldsymbol{T}$ we get $\tilde{\boldsymbol{T}}$.

A very important issue is the cost of solving the AP, i.e., the cost of the convolution (35). In general, a convolution formula of type (35) won't lead to a very efficient numerical algorithm. Indeed, the number of nodes in the set $\mathbb{M}^+$ is $\sim N^3$, where N is the grid dimension in one direction. If the number of nodes n where the solution needs to be known is also $\sim N^3$, then the complexity of summation (35) will be $\sim N^6$, i.e., quadratic with respect to the dimension of the 3D grid. However, for computing Calderon's operators a much better efficiency of implementation can be achieved because of the special structure of the RHS and the solution. Even though the summation in (35) is formally done across the entire grid $\mathbb{M}^+$, in fact, the RHS $g_{\mathbb{M}}$ differs from zero only near γ, see formula (27), which is $\sim N^2$ rather than $\sim N^3$ nodes. Moreover, the solution of the AP needs to be known also only on γ and at the corners, which is again $\sim N^2$ nodes. Hence, the complexity of solving the AP one time will be no more than $\mathcal{O}(N^4)$ in any event.

In fact, this general cost is further reduced due to the special choice of the basis. Recall, each basis vector has only one non-zero component, see (43), i.e., for computing each column of $\boldsymbol{P}_{\gamma^-\gamma^-}$ or $\boldsymbol{P}_{\gamma^+\gamma^-}$ there will be only one non-zero value on γ. Consequently, the RHS $g_{\mathbb{M}}$ of (27) will differ from zero in at most a few neighboring nodes, and the cost of solving the corresponding AP by convolution (35) will be $\mathcal{O}(N^2)$. Altogether, the AP needs to be solved $\sim N^2$ times, because the number of basis vectors is equal to the number of nodes in γ, which is $\sim N^2$. Consequently, the overall cost of solving *all the APs* and computing the matrix of the Calderon operator is $\mathcal{O}(N^4)$.

As demonstrated by the numerical experiments of Section 3, the use of the ABC (41) leads to a substantial improvement in the quality of the solution. Since, however, the computational complexity $\mathcal{O}(N^4)$ is still super-linear (a truly linear complexity would have been $\mathcal{O}(N^3)$), for higher dimensions it is desirable to have it reduced further. This can be achieved by choosing a different basis instead of (43), and using acceleration strategies for computing the convolution (35), see Section 4.2.

3. Numerical experiments

3.1. Grad–Shafranov computations

Since the implementation of the ABC is for a single block of the *MACH3* grid, the FRC must be initialized into a square prism. The equilibrium is adjusted with sufficient open magnetic flux, so the axisymmetric separatrix does not contact any of the block boundaries. The equilibrium is rotated about the axis and projected onto the single-block *MACH3* Cartesian grid. Since the Grad–Shafranov Eq. (10) provides a relationship for the plasma pressure gradient, the background value, see formula (11), is arbitrary. The Grad–Shafranov equilibrium can have zero pressure on the open field line region. *MACH3* cannot model perfect vacuum regions; therefore, a finite, uniform background pressure is set to 20% of the maximum pressure. The pressure profile, formula (11), is then expressed as

$$p(\psi) = \begin{cases} p_{max}(4\psi^2+1)/5 & \text{for} \quad \psi \geqslant 0, \\ p_{max}/5 & \text{for} \quad \psi < 0. \end{cases} \tag{44}$$

The Calderon approach (41) allows one to model the correct physical setting — when the parabolic equation of magnetic diffusion inside the plasma region, see (7), transitions into the Laplace equation (elliptic) for the magnetic field in the surrounding vacuum region, see (13). Formally, this transition corresponds to taking an infinitely large coefficient of magnetic diffusion. Hence, in order to validate the Calderon approach for a steady-state or quasi-steady FRC, we need to be able to apply a vacuum resistivity model in *MACH3*. Such a model assumes that below a certain value of plasma density, there is a (vacuum) region in which anomalous (artificially high) resistivity can be applied. Therefore, we need to obtain a stable FRC with a variable density profile. To this end, a series of simulations has been carried out using the Grad–Shafranov code to obtain an ideally stable equilibrium with a variable density profile.

Since the Grad–Shafranov Eq. (10) relates the plasma pressure distribution to the magnetic field topology and magnitude, the density profile is arbitrary. Specifying a density gradient that is proportional to the pressure gradient is a reasonably accurate assumption and generally matches experimental measurements. The density profile is then set as

$$\rho(\psi) = \begin{cases} \rho_{max}(\psi^2 + 1)/2 & \text{for} \quad \psi \geqslant 0, \\ \rho_{max}/2 & \text{for} \quad \psi < 0, \end{cases} \tag{45}$$

where the background density is set to 50% of the maximum density. This simple approach, however, produces unsatisfactory results with the vacuum resistivity model in *MACH3*.

The plasma pressure and, therefore, the density have a constant background value outside of the separatrix of the FRC. The vacuum resistivity model in *MACH3* is triggered by a density floor value. If that floor value is set exactly equal to the background density value, then the resistivity is ambiguous since in this case, the vacuum state is determined entirely by the finite accuracy of the computational calculations. If the floor value is set below the background density value, then the vacuum resistivity is never triggered. If the floor value is set above the background density value, then the artificially high resistivity region extends inside the FRC separatrix, which causes the equilibrium to decay rapidly.

The issue is resolved by using a density profile with a separatrix that is slightly expanded beyond the separatrix of the pressure equilibrium. The density distribution starts with the distribution given by Eq. (45), and then a diffusion equation is applied to the density to allow it to diffuse beyond the pressure distribution. The resulting pressure and density distributions are shown in Fig. 4 and Fig. 5. The equilibrium temperature distribution is set such that the product of the density and temperature distributions is consistent with the pressure distribution calculated from the Grad–Shafranov equation (10).

The equilibria used for the simulations in this work have a peak temperature of 85 eV, a peak magnetic field of 1.5 T, and a corresponding plasma beta of 51%. The plasma beta is defined as the plasma pressure above background averaged over the closed flux volume and normalized by the maximum magnetic pressure:

$$\beta \equiv \frac{\langle p \rangle}{B_{max}^2/2\mu_0}.$$

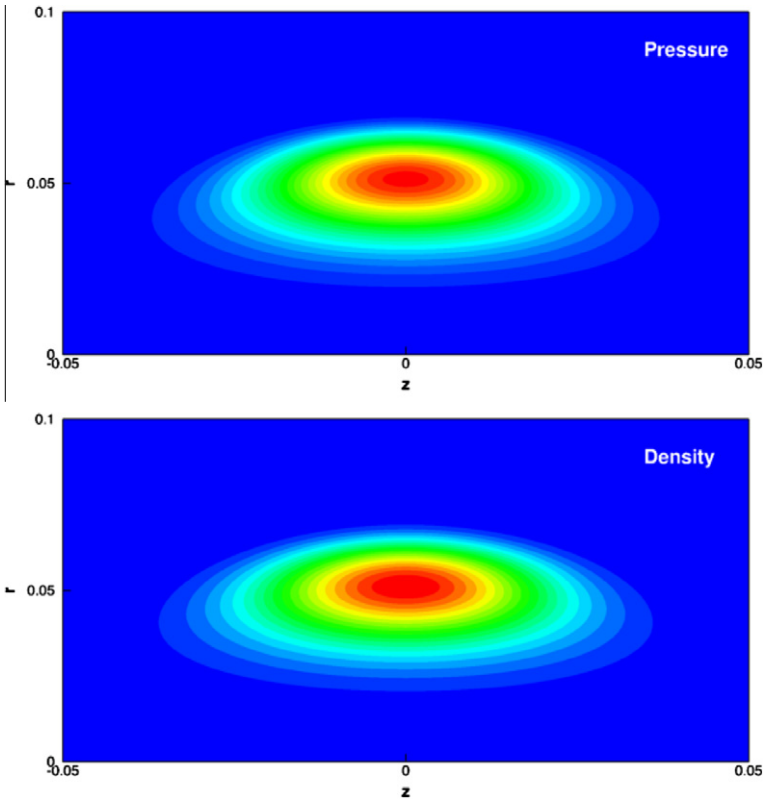

Fig. 4. Equilibrium contours of the plasma pressure and density from the Grad–Shafranov solver, see Eq. (10). The separatrix of the density has been expanded beyond the separatrix location of the pressure and magnetic equilibrium. The differences are slight and are more visible in Fig. 5.

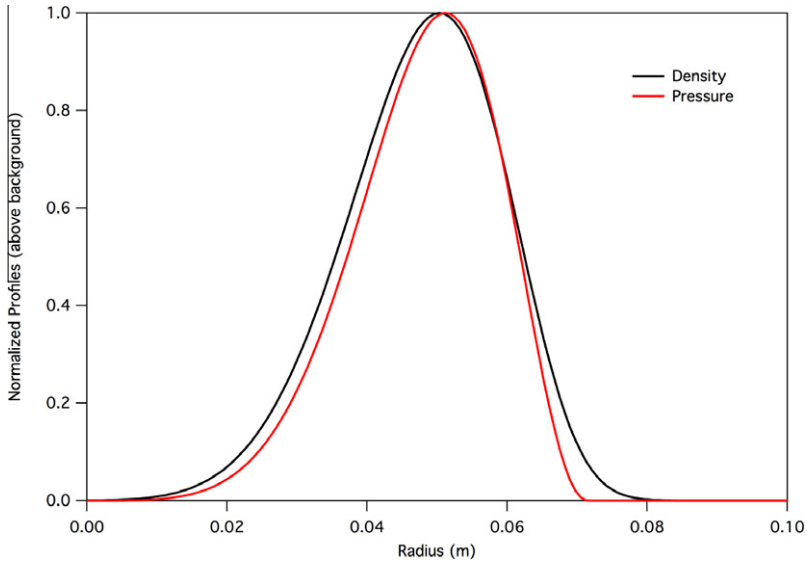

Fig. 5. Equilibrium profiles of the plasma pressure and density along the FRC midplane showing a slightly broader profile for the density.

The theoretical growth time for any MHD instability that might occur is equal to the transit time of an Alfvén wave across the wavelength of the mode. For a plasma density of 10^{-4} kg/m^3, the Alfvén speed is 1.4×10^5 m/s, which gives an MHD growth time of 360 ns for a 0.05 m wavelength.

3.2. Problem setup in MACH3

MACH3 was initialized with an FRC calculated from the Grad-Shafranov Eq. (10). Two configuration sizes have been studied — one with a separatrix radius of the FRC ~3 cm, and the other with the radius ~5 cm. Computations have been carried our in square prism domains of different sizes (typical domain sizes ranged from $6 \times 6 \times 4$ cm to $27 \times 27 \times 18$ cm) and different grid dimensions (typical grid dimensions ranged from $31 \times 31 \times 21$ to $91 \times 91 \times 61$).

Using a cylindrical-to-Cartesian mapper, we have mapped the Grad–Shafranov equilibrium onto a single-block *MACH3* Cartesian grid. Typical equilibrium profiles obtained in a $27 \times 27 \times 18$ cm domain and in a $18 \times 18 \times 12$ cm domain (with a $91 \times 91 \times 61$ grid) are shown in Fig. 6 for the FRC with the separatrix radius of approximately 5 cm. The maximum plasma density value is $\sim 10^{-4}$ kg/m^3 and the background (floor) value is $\sim 5 \times 10^{-5}$ kg/m^3. The profiles of the type shown in Fig. 6 have been used as initial conditions for both the ideal (no resistivity) and resistive simulations. Recall, one needs those non-uniform density profiles for the FRC (Section 3.1) to be able to employ the resistivity model in *MACH3*, with the resistivity that can be set to some large value for the regions in which the density drops below a certain threshold ($\sim 5.5 \times 10^{-5}$ kg/m^3).

We have used conventional wall boundary conditions for hydrodynamic variables (zero normal velocity and zero normal gradients of pressure and density) and three different types of boundary conditions for the magnetic field:

1. Fixed Dirichlet boundary conditions, where the values of the magnetic field from the initial equilibrium are held constant;
2. Neumann, or continuity, boundary conditions, where the magnetic field is assumed to have zero normal derivative at the domain boundaries; and
3. Calderon boundary conditions, where the boundary field is separated into an externally applied magnetic field and a component due to internal plasma currents.

The Dirichlet boundary conditions were used for steady-state (ideal) computations, and the Neumann boundary conditions were used for decaying (resistive) simulations. The Calderon boundary conditions have been used for both steady-state and decaying simulations.

Recall that our implementation of Calderon's boundary conditions allows for the presence of an externally applied magnetic field (see Section 1.4). The implementation is based on a net magnetic field at the boundaries of the domain that can be considered a superposition of the field generated inside the plasma (outgoing) with the given exterior (incoming) magnetic field, e.g., that from the external coils. As described in Section 2.4, prior to applying the Calderon boundary condition, the exterior magnetic field is subtracted from the total magnetic field at the inner part of the grid boundary γ^+. Then, the Calderon boundary condition defines the interior component of the magnetic field at the outer part of the grid boundary γ^- (i.e., at the ghost nodes), after which the exterior field is added back. In doing so, the coil (exterior) magnetic field is computed by integrating the axial component of the overall magnetic field according to Eq. (42). The resulting coil field in Cartesian coordinates is $\boldsymbol{B}^{(\mathrm{inc})} = [0, 0, B_z^{(\mathrm{inc})}]$, with $B_z^{(\mathrm{inc})}$ being a constant value, $B_z^{(\mathrm{inc})} = -0.89$ T for the simulations presented in this work.

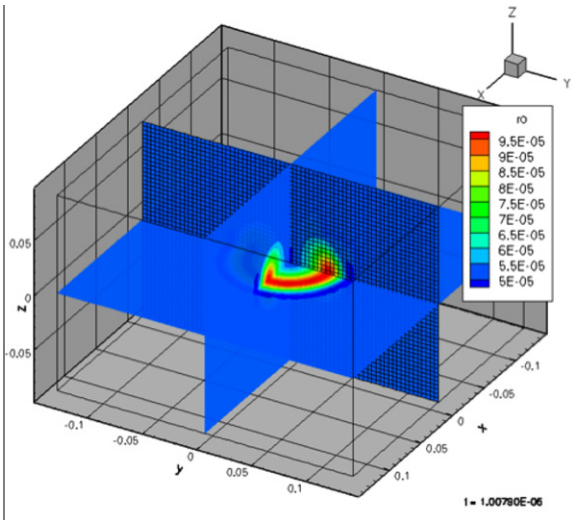

(a) Density on a $27 \times 27 \times 18$ cm domain

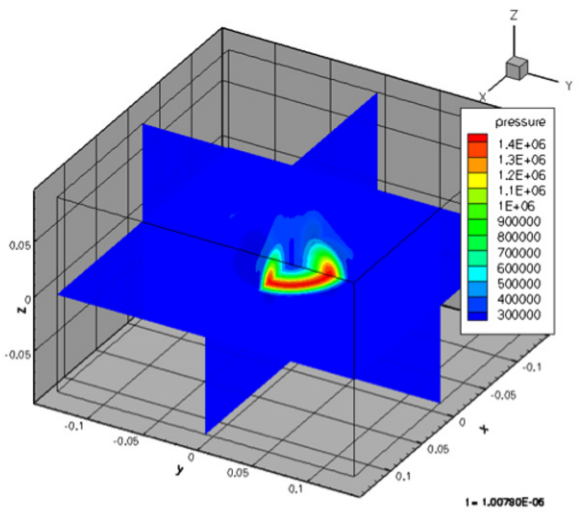

(b) Pressure on a $27 \times 27 \times 18$ cm domain

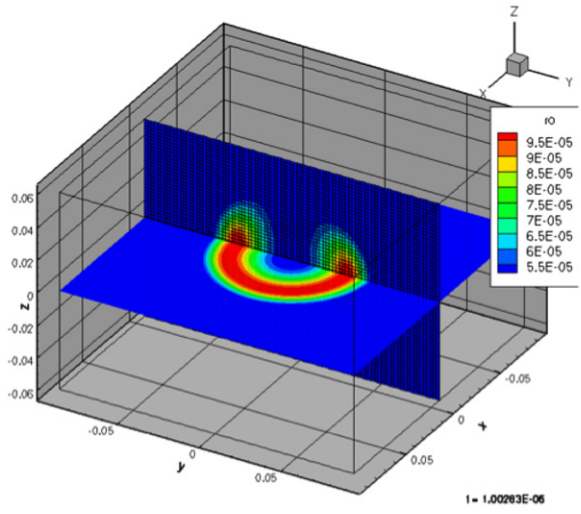

(c) Density on a $18 \times 18 \times 12$ cm domain

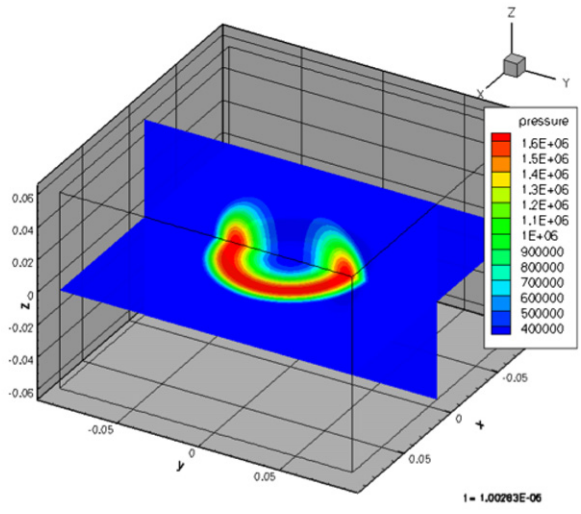

(d) Pressure on a $18 \times 18 \times 12$ cm domain

Fig. 6. Typical *MACH3* equilibrium profiles used in our simulations as initial conditions.

3.3. Results of simulations

In this section, we describe the results of *MACH3* simulations using the Grad–Shafranov equilibrium profiles as initial conditions. We investigate both the case of zero resistivity (ideal plasma) and the case of a finite resistivity.

3.3.1. Ideal simulations

We first present the results of ideal simulations, for which the resistivity of the plasma has been set to zero everywhere in the computational domain. We have observed that for the times of up to $\sim$1 μs the plasma remained stable. At the time of about 1.5 μs, the so-called interchange (or Rayleigh–Taylor) instability starts to develop. A series of test cases have been run to study this phenomenon.

We have corroborated that this instability takes place for different grid resolutions and for both Dirichlet and Calderon boundary conditions. Moreover, we have employed the anomalous vacuum resistivity model, in which the resistivity is large (10^8 Ω· m) on the region with plasma density below the threshold value of 5.5×10^{-5} kg/m^3, and the resistivity is zero, i.e., the plasma is ideal, in the FRC core, where the density is above this threshold. For this case as well, we have observed the development of the same instability. In general, we have found that by the time of approximately 2 μs a strong interchange instability is already fully developed, and in Fig. 7 we are showing the corresponding results on a fine grid of $91 \times 91 \times 61$

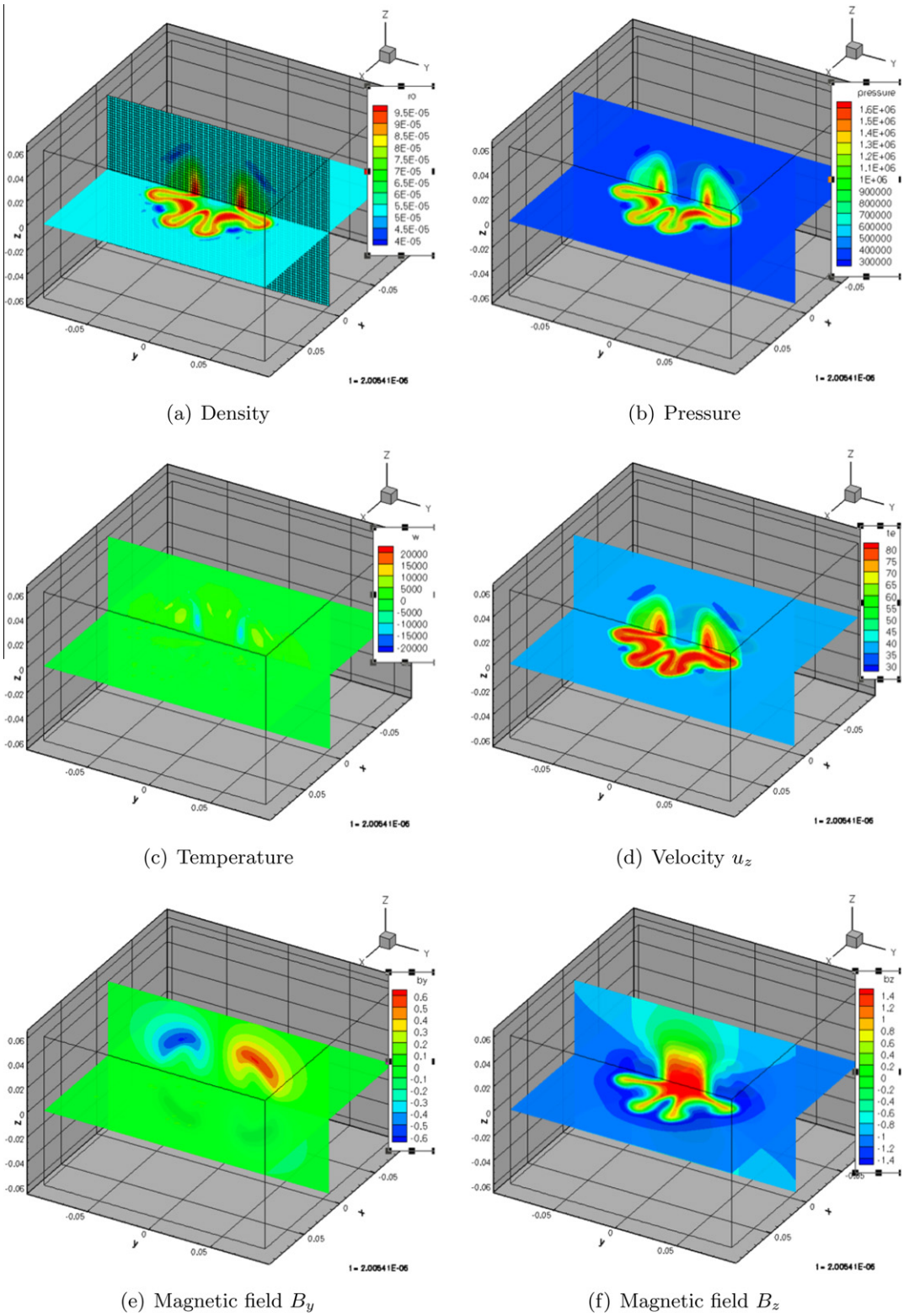

(a) Density (b) Pressure

(c) Temperature (d) Velocity u_z

(e) Magnetic field B_y (f) Magnetic field B_z

Fig. 7. Results of *MACH3* simulations of the ideal FRC on a $18 \times 18 \times 12$ cm domain for $t = 2$ μs.

nodes. At later times ($\gtrsim 3 - 5$ μs), the plasma is completely destroyed. The time of the onset of the Rayleigh–Taylor instability correlates well with the estimate of 360 ns for the development of ideal MHD instabilities.

3.3.2. Resistive simulations

As the ideal FRC equilibria have proven prone to the Rayleigh–Taylor instability developing for the times beyond 1 μs regardless of how the vacuum region is modeled, see Section 3.3.1, we have decided to consider a lossy plasma inside the FRC as well, while still using the anomalous vacuum resistivity model. The vacuum resistivity is set at three orders of magnitude higher than that of the FRC, 10^8 Ω·m and 10^5 Ω· m, respectively. We have assumed a constant magnetic field due to the coils: $\boldsymbol{B}^{(\mathrm{inc})} = [0, 0, B_z^{(\mathrm{inc})}]$, where $B_z^{(\mathrm{inc})} = -0.89$ T, employed either Neumann or Calderon boundary conditions, and used computational domains of several different sizes. The initial profiles of density and B_z are shown in Fig. 8 for the domain size of $12 \times 12 \times 8$ cm.

In the case where the plasma inside the FRC is resistive (i.e., lossy) the initial equilibrium shown in Fig. 8 decays as the time elapses. Specifically, the plasma current gradually vanishes, while both its pressure and density become uniform. The components B_x and B_y of the magnetic field also vanish, while its component B_z is supposed to approach the coil value (constant).

The idea of comparing the performance of the Neumann and Calderon boundary conditions is to simulate the resistive decay of the FRC using computational domains of various sizes. Accordingly, in addition to the small domain of size $12 \times 12 \times 8$ cm, see Fig. 8, we have computed the same solution on a larger domain of size $18 \times 18 \times 12$ cm. In the case of Calderon boundary conditions, the interior solution should not be noticeably affected by the domain size, because these boundary conditions accurately take into account the correct physical behavior of the exterior solution.

As we expect that $[B_x, B_y, B_z] \to [0, 0, B_z^{(\mathrm{inc})}]$ when $t \to \infty$, we use the L_∞ norm of the error for B_z and B_x as a quantitative measure of how accurate the solution is at a given moment of time, and how rapidly it approaches the corresponding asymptotic value. The L_∞ norms are defined as $\max|B_z - B_z^{(\mathrm{inc})}|$ and $\max|B_x|$, respectively, where the maximum is taken over the entire domain/grid. In Figs. 9 and 10 we plot those norms as functions of time for the small domain, and in Figs. 11 and 12 we present similar plots for the large domain. In doing so, we use a logarithmic scale for the vertical axis, which allows us to see the time evolution of the error clearly.

Figs. 9 and 10 show that if the Calderon boundary condition is used for computations on the small domain, $12 \times 12 \times 8$ cm, then the errors for both B_z and B_x approach zero as the time elapses. However, for the Neumann boundary condition the errors flatten far away from zero and do not decay any further. In other words, whereas in the case of the Calderon boundary condition the solution for a lossy FRC converges to its correct asymptotic values as $t \to \infty$, in the case of the Neumann boundary condition the solution converges to incorrect asymptotic values. The discrepancy is substantial: instead of the coil value of $B_z^{(\mathrm{inc})} = -0.89$ T, the magnetic field B_z in the case of the Neumann boundary condition converges to approximately -0.68 T.

Figs. 11 and 12 demonstrate basically the same type of error behavior for the large domain, $18 \times 18 \times 12$ cm. Whereas the error for the Calderon boundary condition converges to zero, the error for the Neumann boundary condition does not. Of course, there is a quantitative difference between the large and small domain, as the Neumann error for the small domain flattens much earlier than it does for the large domain, compare Fig. 9(a) with 11(a), and Fig. 10(a) with 12(a). However, qualitatively the solution obtained with the help of the Neumann boundary condition remains somewhat incorrect even for the large domain. We can therefore conclude that if the Calderon boundary condition is used, then the solution for a lossy FRC is invariant with respect to the domain size, while if the Neumann boundary condition is used, the solution depends on

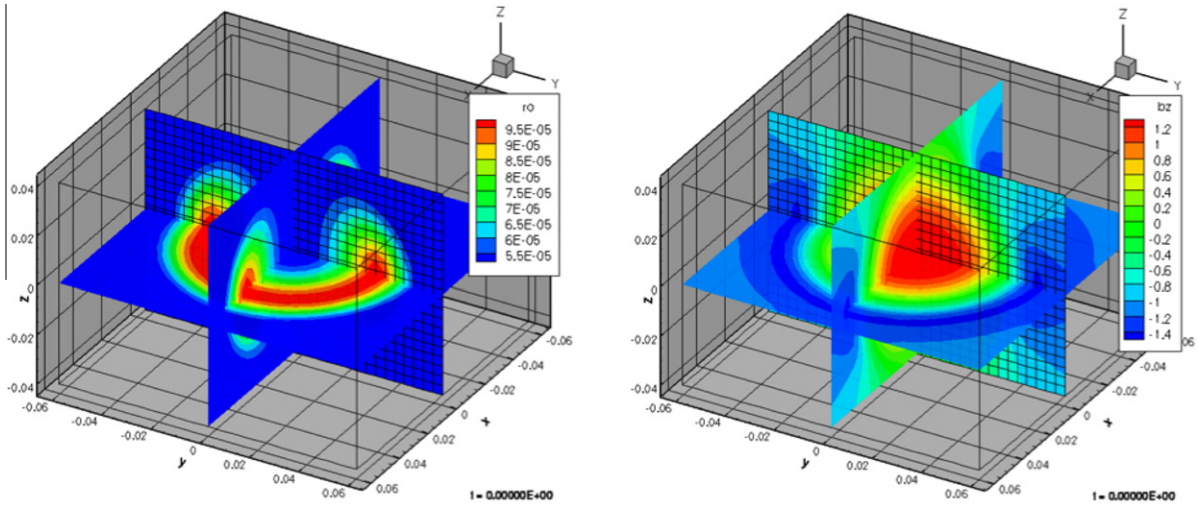

(a) Density (b) Magnetic field B_z

Fig. 8. Initial profiles used for the resistive FRC simulations on the $12 \times 12 \times 8$ cm domain with a $31 \times 31 \times 21$ grid.

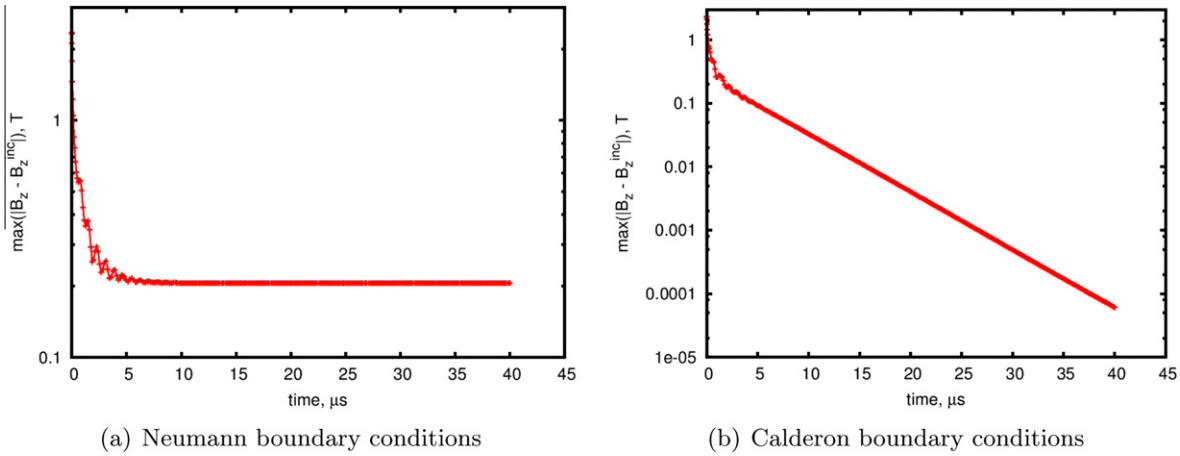

Fig. 9. Time evolution of the norm $\max |B_z - B_z^{(\mathrm{inc})}|$ on a $12 \times 12 \times 8$ cm domain.

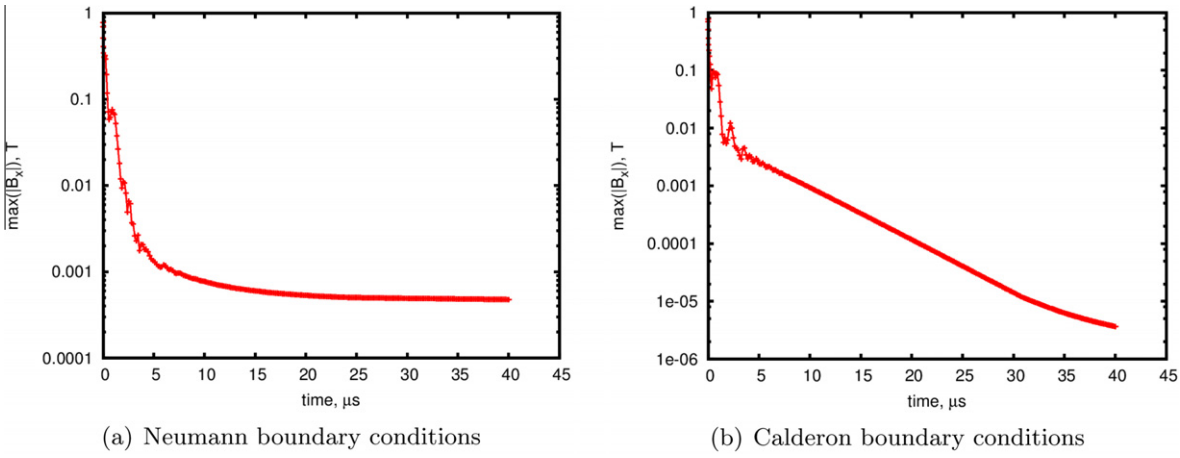

Fig. 10. Time evolution of the norm $\max |B_x|$ on a $12 \times 12 \times 8$ cm domain.

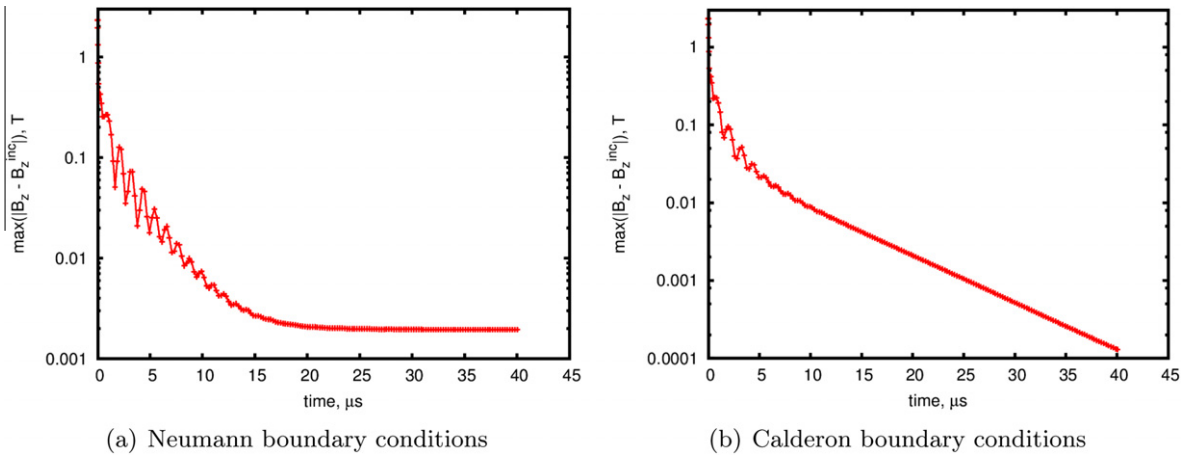

Fig. 11. Time evolution of the norm $\max |B_z - B_z^{(\mathrm{inc})}|$ on a $18 \times 18 \times 12$ cm domain.

the domain size. It is less accurate on the small domain than on the large one, but on the large domain some residual error still remains at convergence.

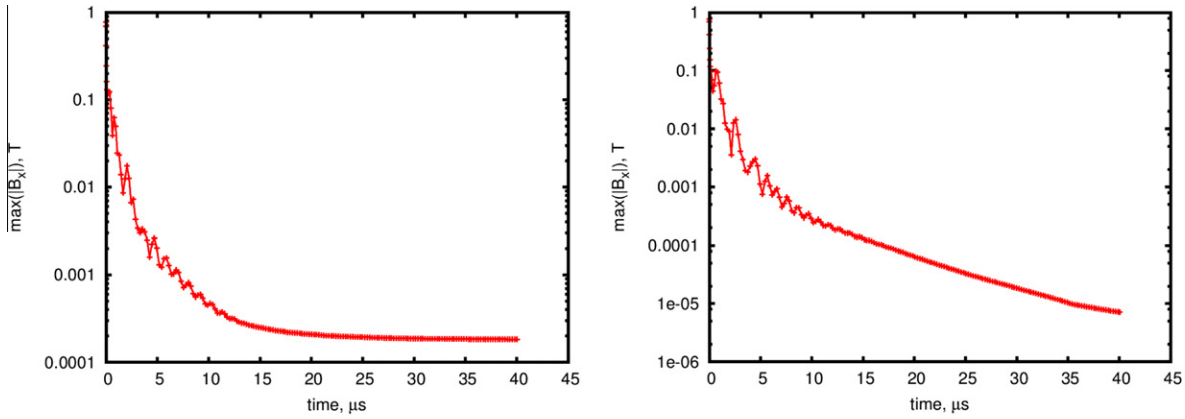

(a) Neumann boundary conditions (b) Calderon boundary conditions

Fig. 12. Time evolution of the norm $\max|B_x|$ on a $18 \times 18 \times 12$ cm domain.

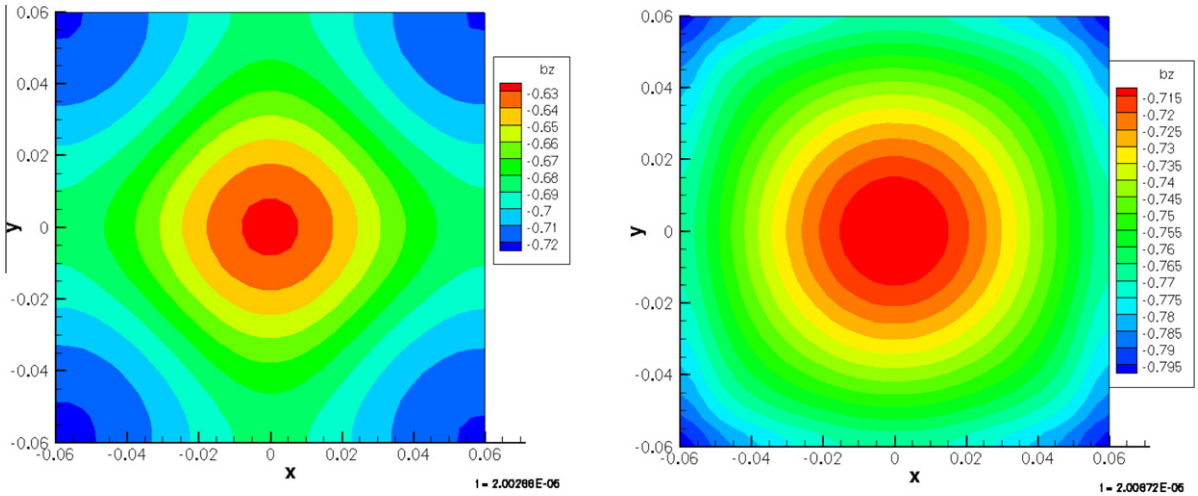

(a) Neumann boundary conditions (b) Calderon boundary conditions

Fig. 13. Contours of B_z in the (x,y) plane for the small domain at $t = 2 > \mu s$.

Additional evidence of a qualitative disagreement between the solutions obtained using two types of boundary conditions is provided by the contour plots in Fig. 13. The contours in Fig. 13(a) that correspond to the Neumann boundary condition clearly indicate that the solution has lost its axial symmetry, whereas the contours in Fig. 13(b) that correspond to the Calderon boundary condition still remain nearly circular, as it is supposed to be in the axially symmetric case. Altogether we conclude that the Calderon boundary condition demonstrates a superior performance over the traditional approach that employs the Neumann boundary condition.

4. Discussion

4.1. Accomplishments of the current work

Using Calderon's operators, we have designed and implemented an advanced nonlocal ABC for simulating the quasi-static magnetic field exterior to a plasma FRC. This ABC provides a viable alternative to the current practice of computing such configurations that requires a large vacuum region modeled with the help of an artificially high magnetic diffusion. Specifically, the new Calderon ABC enables high simulation accuracy on small computational domains that involve practically no "white space" beyond the separatrix of the FRC. The design properties of the new ABC were corroborated experimentally by computing several FRC solutions with the help of the code *MACH3*. In particular, the outer boundary of the small domain that we have used, $12 \times 12 \times 8$ cm, was only 1 cm away from the FRC whose diameter was approximately 10 cm.

4.2. Possible future extensions

Having verified that the Calderon ABC indeed enables a better accuracy of the numerical solution on small domains, we can identify the following directions for the future work. Implementation of the ABC in a multi-block setting will offer a very important new capability, as multi-block grids are used extensively for obtaining accurate problem-specific discretizations. In the case where the outer boundary is composed of several patches belonging to different blocks, the key issue will be that of minimizing the inter-block communication needed for maintaining the global structure of the Calderon ABC. Likewise, implementation of the ABC with other MHD codes will be equally important, as other codes may offer additional capabilities from the standpoint of physics. For example, the code *WARPX* employs a two-fluid plasma model, see [18–20], as opposed to *MACH3* that is based on a single fluid plasma model.

In the context of the formulation investigated in this paper, it would be interesting to include the possibility of adding the discrete external field coils, and of having those coils driven by time-dependent currents (still varying slowly, so that the quasi-static far-field model stays valid).

On the theoretical/algorithmic side, the computation of Calderon's operators can be further sped up if a different basis for representing the operators is chosen instead of the simplest point-wise basis (43) used in Section 2.2. For example, one can use the traces of Chebyshev polynomials on the grid as basis functions, and in doing so expect that on fine grids considerably fewer polynomials than grid nodes will be needed for achieving a comparable accuracy. Moreover, the computation of discrete convolutions (35) can be substantially accelerated by applying a discrete version of the well-known fast multipole method (FMM) [21]. Its basic principles remain the same as in the continuous case [22]: far-field contributions to the potential due to remote sources are computed via a multipole expansion, while the near field is computed directly. To that end we note that the far field in the proposed methodology essentially does not change compared to the continuous case; this follows immediately from the construction of the discrete fundamental solution $G^{(h)}$, see Appendix C. The difference between the discrete and continuous fundamental solution may be substantial only in the near field. This, however, does not affect the FMM since the near-field contribution to the potential is evaluated directly anyway.

In addition to the direct method employed in this work, other potentially useful methods for solving the BEP, i.e., for solving system (36), may involve iterations, or, alternatively, the QR or SVD decomposition. Finally, other geometries besides the Cartesian may provide a better fit for a given formulation. For example, cylindrical geometry is often used for computing the plasma FRCs. One can show that Calderon's operators can be computed efficiently for cylindrical outer boundaries. Namely, using the simplest basis similar to that of Section 2.2, one can obtain the overall complexity of $\mathcal{O}(N_z^3 N_\theta \ln N_\theta)$ operations, where N_z is the number of nodes in the axial direction and N_θ is the number of nodes in the circumferential direction. In doing so, one takes advantage only of a symmetric shape of the boundary (a body of revolution) and does not assume that the solution is axially symmetric (i.e., the solution can remain fully 3D).

Appendix A. Applicability limits for the single fluid MHD

The first step toward understanding the applicability limits for the single fluid MHD is to look into the behavior of small perturbations on top of a given background or, more precisely, to consider linear waves and analyze their frequencies and wavenumbers (wavelengths). The corresponding analysis is standard in the literature, see, e.g. [23–28]. Three types of waves are normally identified in single fluid plasmas: the Alfvén waves, magnetoacoustic waves, and ion sound. The latter two can only be considered separately if the thermodynamic speed of sound $c_s = \sqrt{\frac{\gamma p_0}{m_i n_0}}$ happens to be much slower than the Alfvén speed $c_A = \sqrt{\frac{B_0^2}{4\pi m_i n_0}}$ (the parameters with subscript "0" in the definitions of both speeds are background parameters). What is most important though is that for all types of linear waves their frequency ω appears proportional to the wavenumber k : $\omega \propto k$ (although the value of the proportionality constant may depend on the direction in space, i.e., there is room for anisotropy caused by the external magnetic field). This direct proportionality between ω and k is commonly referred to as the linear dispersion law and essentially implies that all linear waves in the single fluid MHD are dispersionless. This means that both their phase speed $\frac{\omega}{k}$ and their group speed $\frac{\partial \omega}{\partial k}$ are constant (in a given direction) and do not depend on either ω or k.

The dispersionless nature of linear waves in the single fluid MHD basically means that there are no characteristic frequencies in this model, and speaking formally, both ω and k can be arbitrarily high. One can, however, reformulate the previous question as follows: How high may the frequency and the wavenumber actually be so that to still keep the results physical? This question, of course, cannot be answered from within the single fluid framework. To address it, one rather needs to analyze the properties of linear waves in a more comprehensive plasma model.

The next, more comprehensive, model is known as the two fluid MHD. The electrons and ions are considered as two mutually penetrating fluids, each in the state of its own thermodynamical equilibrium (no kinetic considerations yet). The momentum equations are written independently for each fluid; in particular, the full momentum equation for the electrons reads:

$$m_e n \frac{d\boldsymbol{u}_e}{dt} + \operatorname{grad} p_e = -en\boldsymbol{E} - \frac{en}{c}\boldsymbol{u}_e \times \boldsymbol{B} - \frac{m_e n}{\tau}(\boldsymbol{u}_e - \boldsymbol{u}_i), \tag{46}$$

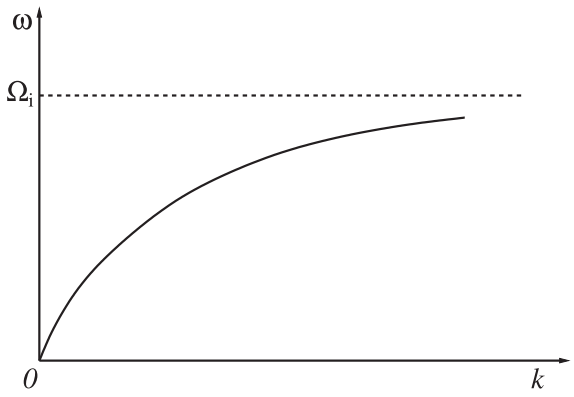

Fig. 14. Dispersion of Alfvén waves.

where $-e$ is the electron charge and τ is the average time between electron–ion collisions. If the electron inertia is still neglected, then Eq. (46) transforms into the generalized Ohm law:

$$\operatorname{grad} p_e = -en\boldsymbol{E} - \frac{en}{c}\boldsymbol{u}_i \times \boldsymbol{B} + \frac{1}{c}\boldsymbol{j} \times \boldsymbol{B} + \frac{en\boldsymbol{j}}{\sigma}, \tag{47}$$

where the current density is given by $\boldsymbol{j} = en(\boldsymbol{u}_i - \boldsymbol{u}_e)$ and the conductivity is $\sigma = \frac{e^2 n\tau}{m_e}$. Note that if an equation similar to (46) is written for the ions, and the two equations are added together under the assumption that $m_e = 0$, then one arrives back at Eq. (1).

Unlike in the single fluid model, all linear waves in the two fluid MHD become dispersive. Depending on a particular branch of oscillations, it may either be sufficient to use the generalized Ohm law (47) or one may need to fully take into account the inertia of the electrons (46) to analyze the dispersive behavior. The analysis, again, is standard in the literature, see, e.g., [23–25]. For example, an Alfvén wave that propagates almost transversely with respect to the direction of the background magnetic field $\boldsymbol{B}_0$ so that $k_\parallel^2 \ll k^2$, has the following dispersion relation:

$$\omega^2 = c_A^2 k_\parallel^2 \frac{\Omega_i^2}{\Omega_i^2 + c_A^2 k_\parallel^2}, \tag{48}$$

where $\Omega_i = \frac{eB_0}{m_i c}$ is the ion cyclotron (or Larmor) frequency. The corresponding dependence $\omega = \omega(k)$ is schematically represented in Fig. 14. From this figure and from formula (48) we see that the linear dispersion relation $\omega \propto k$ that characterizes the single fluid model can only be considered an approximation for the initial part of the frequency interval $[0, \Omega_i]$, i.e., for the frequencies $\omega \ll \Omega_i$.

Dispersion relations for other linear waves are similar. For example, a transverse magnetoacoustic wave has the dispersion relation (obtained by taking into account the inertia of the electrons):

$$\omega^2 = c_A^2 k^2 \frac{\omega_{pe}^2}{\omega_{pe}^2 + c^2 k^2}, \tag{49}$$

where $\omega_{pe} = \sqrt{\frac{4\pi e^2 n_0}{m_e}}$ is the plasma electron (or Langmuir) frequency. As $k \to \infty$ in formula (49), we have $\omega \to c_A \omega_{pe}/c = \sqrt{\Omega_e \Omega_i}$, where $\Omega_e = \frac{eB_0}{m_e c}$ is the electron cyclotron frequency, and $\sqrt{\Omega_e \Omega_i}$ is known as the lower hybrid frequency. The single fluid model can therefore be considered a good approximation for the frequency range $\omega \ll \sqrt{\Omega_e \Omega_i}$.

We refer the reader to [23–28] for a detailed analysis of the dispersion of linear waves in plasma. The overall conclusion is that while the single fluid MHD has no characteristic frequencies of its own, the linear dispersion relation will remain valid only for those frequencies ω that are much lower than all the characteristic frequencies in more comprehensive models. The lowest of the latter are typically the plasma ion frequency $\Omega_{pi} = \sqrt{\frac{4\pi e^2 n_0}{m_i}}$ and the ion cyclotron frequency Ω_i, and it is them that present the most limiting constraint on the admissible range of ω. It is precisely this range of frequencies that quantifies the notion of low frequencies, for which the single fluid approximation holds and provides the trustworthy results. The corresponding wavenumbers $k = k(\omega)$ quantify the foregoing notion of a large scale.

Appendix B. Frequency dependent vs. quasi-static ABCs

The quasi-static interpretation of the exterior field $\boldsymbol{B}$, see formulae (13), (14), means that we can think of an infinite wavelength or infinite propagation speed outside D. In reality, of course, neither of that is true. If we kept the displacement current in the Ampère law, i.e., if we wrote

$$\frac{1}{c}\frac{\partial \boldsymbol{E}}{\partial t} - \operatorname{curl}\boldsymbol{B} = -\frac{4\pi}{c}\boldsymbol{j}$$

instead of Eq. (3), then we would have obtained a true d'Alembert (wave) equation for $\boldsymbol{B}$:

$$\frac{1}{c^2}\frac{\partial^2 \boldsymbol{B}}{\partial t^2} - \Delta \boldsymbol{B} = \boldsymbol{0} \quad \text{on} \quad \mathbb{R}^3 \setminus D \tag{50}$$

instead of the Laplace equation (13). This would result in the propagation of electromagnetic waves with the speed c and with the wavelengths determined by the frequencies (or, speaking more generally, the characteristic time scales) of the processes going on inside D.

As long as those interior processes are computed by a single fluid MHD code *MACH3*, the corresponding time scales are limited by the considerations outlined in Appendix A. Namely, the frequencies should stay low, or, more precisely, well below all the characteristic frequencies, so that none of the linear waves may become dispersive.

Typical FRC parameters achieved in the experiments may vary slightly between different sources in the literature, see, e.g. [29–31]. Quoting [29], we have: $n_0 \sim 5\times 10^{13}$–5×10^{15} cm^{-3}, $B_0 \sim 0.75$–0.95 kG, $T_\mathrm{i} \sim 3$ keV, $T_\mathrm{e} \sim 500$ eV. Based on these parameters, we can estimate the characteristic frequencies mentioned in Appendix A. The lowest one is the Larmor frequency for ions Ω_i, and to make sure that the simulations conducted with the help of *MACH3* produce physical results, we must have $\omega \ll \Omega_\mathrm{i}$. Taking the midpoint value for the magnetic field, $B_0 \approx 0.85$ kG, we obtain $\Omega_\mathrm{i} \approx 8.1\times 10^6$ s^{-1}. The corresponding wavelength in vacuum, i.e., on $\mathbb{R}^3 \setminus D$, is $\lambda_\mathrm{i} = \frac{2\pi c}{\Omega_\mathrm{i}} \approx 2.33\times 10^5$ cm, which is over two kilometers, and the requirement $\omega \ll \Omega_\mathrm{i}$ translates into having $\lambda \gg \lambda_\mathrm{i}$ on $\mathbb{R}^3 \setminus D$. Such wavelengths, in particular, are much larger than the domain size diam$D$, and we are going to show that in this regime the frequency dependent ABCs reduce to the quasi-static ones.

B.1. Frequency dependent ABCs

Let us assume for a moment that the computational domain $D \subset \mathbb{R}^3$ has the form of a ball of radius R_0, and let the propagation of waves outside this ball be governed by the homogeneous d'Alembert equation (50). We will construct the exact analytic ABCs at the external artificial boundary $r = R_0$. The ABCs will guarantee the reflectionless propagation of all the outgoing waves through the outer boundary, so that the solution inside the computational domain $r \leqslant R_0$ be the same as if the original problem was first solved on the entire $\mathbb{R}^3$ and then its solution truncated.

The signal governed by Eq. (50) is normally assumed broadband, and we will analyze its individual constituent frequencies. For a given frequency ω, the d'Alembert equation (50) transforms into the Helmholtz equation for each Cartesian component B of the field $\boldsymbol{B}$:

$$\Delta B + k^2 B = 0, \tag{51}$$

where the wavenumber k is given by $k = \omega/c$. As Eq. (51) is considered on the unbounded region $r \geqslant R_0$, it must be supplemented by the Sommerfeld radiation condition at infinity:

$$\frac{\partial B}{\partial r} + ikB = o(r^{-1}), \quad \text{as} \quad r \to \infty. \tag{52}$$

Solution of Eq. (51) is obtained by the separation of variables:

$$B = \sum_{l=0}^{\infty}\sum_{m=-l}^{l} a_{lm}\hat{B}_{lm}(r)Y_l^m(\theta,\varphi), \tag{53}$$

where $Y_l^m(\theta,\varphi)$ are spherical functions, $\hat{B}_{lm}(r)$ are functions of the radius r, and a_{lm} are coefficients. For each pair of indexes (l,m), the function $\hat{B}_{lm}$ satisfies the Bessel equation:

$$\hat{B}''_{lm} + \frac{2}{r}\hat{B}'_{lm} + \left[k^2 - \frac{l(l+1)}{r^2}\right]\hat{B}_{lm} = 0, \tag{54}$$

which means, in particular, that $\hat{B}_{lm} \equiv \hat{B}_l$. The solution $\hat{B}_l(r)$ is considered on the semi-infinite line $r \geqslant R_0$, and should satisfy the Fourier-transformed version of the Sommerfeld condition (52):

$$\hat{B}'_l + ik\hat{B}_l = o(r^{-1}), \quad \text{as} \quad r \to \infty. \tag{55}$$

Eq. (54) has two linearly independent solutions:

$$\hat{B}_l^{(1)}(r) = \frac{1}{\sqrt{r}}H_{l+1/2}^{(1)}(kr) \quad \text{and} \quad \hat{B}_l^{(2)}(r) = \frac{1}{\sqrt{r}}H_{l+1/2}^{(2)}(kr), \tag{56}$$

where $H_{l+1/2}^{(1)}$ and $H_{l+1/2}^{(2)}$ are Hankel functions of the first and second kind, respectively, of semi-integer order. Using asymptotic expressions for the Hankel functions:

$$H_v^{(1)}(x) = \sqrt{\frac{2}{\pi x}} e^{i\left(x - v\frac{\pi}{2} - \frac{\pi}{4}\right)} + O(x^{-\frac{3}{2}}), \quad x \to +\infty,$$
$$H_v^{(2)}(x) = \sqrt{\frac{2}{\pi x}} e^{-i\left(x - v\frac{\pi}{2} - \frac{\pi}{4}\right)} + O(x^{-\frac{3}{2}}), \quad x \to +\infty,$$

one can easily see that only the second solution $\hat{B}_l^{(2)}(r)$ from the fundamental system (56) satisfies the radiation condition (55). We must therefore require that

$$\hat{B}_l(r) \propto \frac{1}{\sqrt{r}} H_{l+1/2}^{(2)}(kr), \quad r \geqslant R_0,$$

which is equivalent to

$$\det \begin{bmatrix} \hat{B}_l & \frac{1}{\sqrt{r}} H_{l+1/2}^{(2)}(kr) \\ \hat{B}_l' & \frac{d}{dr}\frac{1}{\sqrt{r}} H_{l+1/2}^{(2)}(kr) \end{bmatrix} = 0. \tag{57}$$

It is sufficient for the Wronskian in (57) to be equal to zero only at one point, which is convenient to choose as the location of the artificial boundary $r = R_0$. Therefore, we arrive at the following ABCs in the Fourier space:

$$\hat{B}_l' - \hat{B}_l \frac{\frac{d}{dr}\frac{1}{\sqrt{r}} H_{l+1/2}^{(2)}(kr)}{\frac{1}{\sqrt{r}} H_{l+1/2}^{(2)}(kr)}\Big|_{r=R_0} = 0, \quad l = 0, 1, 2, \ldots \tag{58}$$

We will show that in the case of long waves, $kR_0 \ll 1$, boundary conditions (58) for all $l = 0, 1, 2, \ldots$ transform into the corresponding ABCs for the Laplace equation.

B.2. Quasi-static ABCs

Along with the monochromatic wave Eq. (51) consider the scalar Laplace equation:

$$\Delta B = 0, \quad r \geqslant R_0, \tag{59}$$

subject to the condition of vanishing of the solution at infinity:

$$B \to 0 \quad \text{as} \quad r \to \infty. \tag{60}$$

Formulae (59) and (60) are obtained from formulae (13) and (14), respectively, by considering individual Cartesian components of $\boldsymbol{B}$. Eq. (59) governs a stationary field that can be thought of as a limit of what the propagating field becomes when the wavelength increases and the variation of the solution in time slows down.

Solution of the Laplace equation (59) can be represented by the same series (53) as corresponds to the Helmholtz equation (51), except that the functions $\hat{B}_{lm}(r) \equiv \hat{B}_l(r)$ should now satisfy the ordinary differential equation

$$\hat{B}_l'' + \frac{2}{r}\hat{B}_l' - \frac{l(l+1)}{r^2}\hat{B}_l = 0 \tag{61}$$

rather than the Bessel equation (54). Eq. (61) has two linearly independent solutions:

$$\hat{B}_l^{(1)}(r) = r^l \quad \text{and} \quad \hat{B}_l^{(2)}(r) = r^{-(l+1)}, \tag{62}$$

and we immediately see that only $\hat{B}_l^{(2)}(r)$ satisfies condition (60). We must therefore require that

$$\hat{B}_l(r) \propto r^{-(l+1)}, \quad r \geqslant R_0,$$

which is equivalent to

$$\det \begin{bmatrix} \hat{B}_l & r^{-(l+1)} \\ \hat{B}_l' & \frac{d}{dr} r^{-(l+1)} \end{bmatrix} = 0. \tag{63}$$

Consequently, for the Laplace equation we obtain the following ABCs (cf. formula (58)):

$$\hat{B}_l' + \frac{l+1}{r}\hat{B}_l|_{r=R_0} = 0, \quad l = 0, 1, 2, \ldots \tag{64}$$

We will prove that as the size $\operatorname{diam} D = R_0$ of the computational domain D becomes small compared to the wavelength $\lambda = 2\pi/k$, boundary conditions (58) will converge to boundary conditions (64) for all respective values of $l = 0, 1, 2, \ldots$.

B.3. Long waves $\lambda \gg R_0$

Let us begin with recasting ABCs (58) in the form:

$$\hat{B}'_l - \hat{B}_l\left[-\frac{1}{2}\frac{1}{r} + \frac{kH^{(2)\prime}_{l+1/2}(kr)}{H^{(2)}_{l+1/2}(kr)}\right]\Bigg|_{r=R_0} = 0, \quad l = 0, 1, 2, \ldots, \tag{65}$$

where $H^{(2)\prime}_{l+1/2}(\cdot)$ is the derivative of the Hankel function with respect to its argument. In our subsequent analysis, we will need the following representation of Hankel functions (of non-integer order) via Bessel functions:

$$H^{(2)}_{l+1/2}(x) = \frac{1}{i\sin\pi(l+\frac{1}{2})}\left[J_{l+1/2}(x)e^{i\pi(l+\frac{1}{2})} - J_{-l-1/2}(x)\right]. \tag{66}$$

In turn, the Bessel functions of semi-integer order can be represented via elementary functions. We will first consider the case of $l = 0$. Then,

$$J_{1/2}(x) = \sqrt{\frac{2}{\pi x}}\sin x \quad \text{and} \quad J_{-1/2}(x) = \sqrt{\frac{2}{\pi x}}\cos x.$$

Consequently (see formula (66)):

$$H^{(2)}_{1/2}(x) = i\sqrt{\frac{2}{\pi x}}e^{-ix},$$

and therefore,

$$H^{(2)\prime}_{1/2}(x) = i\sqrt{\frac{2}{\pi}}\left[-\frac{1}{2}\frac{1}{\sqrt{x^3}}e^{-ix} - i\frac{1}{\sqrt{x}}e^{-ix}\right].$$

Substituting these expressions into formula (65) for $l = 0$, we obtain:

$$\hat{B}'_l + \hat{B}_l\left[\frac{1}{r} + ik\right]|_{r=R_0} = 0. \tag{67}$$

In the case of long waves $\lambda \equiv 2\pi/k \gg R_0$ we have $k \ll 1/R_0$. Consequently, at the artificial boundary $r = R_0$ the magnitude of the first term in parentheses on the right-hand side of formula (67) greatly exceeds the magnitude of the second term. Hence, boundary condition (67) becomes closer and closer to boundary condition (64) for $l = 0$ as the wavelength increases.

Next, we consider the case $l > 0$. The Bessel functions are represented as follows:

$$\begin{aligned} J_{l+1/2}(x) &= (-1)^l\sqrt{\frac{2}{\pi}}x^{l+\frac{1}{2}}\left(\frac{d}{xdx}\right)^l\frac{\sin x}{x}, \\ J_{-l-1/2}(x) &= \sqrt{\frac{2}{\pi}}x^{l+\frac{1}{2}}\left(\frac{d}{xdx}\right)^l\frac{\cos x}{x}, \end{aligned} \tag{68}$$

and for the derivative of the Hankel function we will employ the recurrence formula:

$$H^{(2)\prime}_{l+1/2}(x) = \frac{1}{2}\left[H^{(2)}_{l-1/2}(x) - H^{(2)}_{l+3/2}(x)\right]. \tag{69}$$

As we are interested in evaluating the Hankel function and its derivative at $x = kR_0 \ll 1$, we will use asymptotic expressions for small x in formulae (68). We have

$$\frac{\cos x}{x} = \frac{1}{x} + O(x),$$

and consequently,

$$J_{-l-1/2}(x) = \sqrt{\frac{2}{\pi}}x^{l+\frac{1}{2}}(-1)^l 1\cdot 3\cdot 5\cdots(2l-1)\frac{1}{x^{2l+1}} + O\left(\frac{1}{x^{l-\frac{1}{2}}}\right).$$

Likewise,

$$\frac{\sin x}{x} = 1 + O(x^2),$$

and consequently,

$$J_{l+1/2}(x) = O\left(x^{l+\frac{1}{2}}\right),$$

which means that $J_{l+1/2}(x)$ can be neglected compared to $J_{-l-1/2}(x)$. Therefore,

$$H^{(2)}_{l+1/2}(x) \approx \underbrace{\frac{1}{i\sin\pi\left(l+\frac{1}{2}\right)}}_{=(-1)^l}\left[-\sqrt{\frac{2}{\pi}}(-1)^l 1\cdot 3\cdot 5\cdots(2l-1)\frac{1}{x^{l+\frac{1}{2}}}\right] = i\cdot 1\cdot 3\cdot 5\cdots(2l-1)\frac{1}{x^{l+\frac{1}{2}}},$$

and, using formula (69),

$$H^{(2)\prime}_{l+1/2}(x) \approx \frac{i}{2}\left[i\cdot 1\cdot 3\cdot 5\cdots(2l-3)\frac{1}{x^{l-\frac{1}{2}}} - i\cdot 1\cdot 3\cdot 5\cdots(2l+1)\frac{1}{x^{l+\frac{3}{2}}}\right].$$

Substituting these expressions into formula (65) for $l > 0$, we obtain:

$$\hat{B}'_l + \hat{B}_l\left[\frac{l+1}{r} - \frac{k}{2}\frac{kr}{2l-1}\right]|_{r=R_0} = 0. \tag{70}$$

As the wavelength becomes large, $kR_0 \ll 1$, boundary condition (70) approximates boundary condition (64) for the respective value of $l > 0$.

B.4. Other geometries

The foregoing proof applies to the case of a spherical artificial boundary, $r = R_0$. However, the problem formulated on the ball $r \leqslant R_0$ can be used in the capacity of an auxiliary problem, see Section 2.1, for computing Calderon's operators for both the Helmholtz and the Laplace equation at the boundary $\Gamma = \partial D$ of an arbitrary shape located inside the sphere $r = R_0$. For example, Γ may be the surface of a parallelepiped introduced and studied in Sections 2.2, 2.3, which is not a separable surface for the Laplace operator. However, the corresponding Calderon boundary equations with projections at the "irregular" boundary Γ will be equivalent to the Helmholtz and Laplace ABCs, respectively, at the spherical boundary $r = R_0$. Hence, the previous result on the convergence of frequency dependent ABCs to quasi-static ABCs for long waves extends to the case of artificial boundaries of a more general shape.

Appendix C. Discrete fundamental solution

The fundamental solution of the finite-difference Laplace operator is defined as the solution $G^{(h)}$ to the following discrete Poisson equation:

$$\Delta^{(h)}G^{(h)} = \begin{cases} \frac{1}{h^3}, & i = j = k = 0, \\ 0, & \text{otherwise}. \end{cases} \tag{71}$$

In addition, the grid function $G^{(h)}$ shall vanish at infinity. In formula (71), $\Delta^{(h)}$ denotes the finite-difference Laplacian, which in the current paper is given by formula (23), and the right-hand side (RHS) is a counterpart of the Dirac δ-function on the grid. The scaling of the RHS is chosen so that when its value at the origin is multiplied by the cell volume, which is h^3, the result will be equal to one. This is analogous to "integrating" the genuine δ-function, which also yields one.

The relation between $G^{(h)}$ and the true fundamental solution of the continuous Laplacian needs to be clarified. In the continuous case, we define the fundamental solution $G(\boldsymbol{x})$ as the solution to the Poisson equation

$$\Delta G = \delta(\boldsymbol{x}) \tag{72}$$

subject to the zero condition at infinity:

$$G(\boldsymbol{x}) \to 0 \quad \text{as} \quad |\boldsymbol{x}| \to \infty. \tag{73}$$

It is well known that the solution of problem (72), (73) is

$$G(\boldsymbol{x}) = -\frac{1}{4\pi|\boldsymbol{x}|}. \tag{74}$$

This function is singular at the origin, and we cannot and should not anticipate that the discrete fundamental solution will approximate it near singularity. Scheme (71) merely looses consistency in the vicinity of $\boldsymbol{x} = \boldsymbol{0}$.

We shall, however, expect that the discrete fundamental solution $G^{(h)}$ will approximate the continuous fundamental solution G well far away from the origin. Therefore, if Eq. (71) is to be solved on a sufficiently large cube:

$$\{-S \leqslant x \leqslant S, -S \leqslant y \leqslant S, -S \leqslant z \leqslant S\}, \tag{75}$$

then we can simply supplement it by the Dirichlet boundary condition with the data provided by expression (74):

$$G^{(h)}|_{i=\pm N} = G^{(h)}|_{j=\pm N} = G^{(h)}|_{k=\pm N} = -\frac{1}{4\pi|\boldsymbol{x}|}. \tag{76}$$

In formula (76), $N = S/h$.

On a given grid, solution of the finite-difference problem (71), (76) needs to be computed only once. This is done by the separation of variables, and in doing so the inhomogeneous Dirichlet condition (76) is equivalently replaced by the additional source term (RHS) next to the boundary. The source term is obtained by subtracting an arbitrary function that satisfies the inhomogeneous condition (76) and then differentiating, i.e., applying the discrete Laplacian $\Delta^{(h)}$. Hence, the boundary condition at all faces of the cube (75) becomes zero Dirichlet, and in each coordinate direction one can expand the solution and the RHS with respect to the trigonometric basis

$$\sin\left(\pi\frac{\phi+S}{2S}\right),\quad \sin\left(2\pi\frac{\phi+S}{2S}\right),\ldots,\sin\left(n\pi\frac{\phi+S}{2S}\right),\ldots, \tag{77}$$

which enables the use of the FFT and thus guarantees efficiency (linear complexity with respect to the dimension of the 3D grid, which is $\sim N^3$). Moreover, as there are obvious symmetries in the problem, it can, in fact, be solved only on one eighth of the cube:

$$\{0 \leqslant x \leqslant S, 0 \leqslant y \leqslant S, 0 \leqslant z \leqslant S\}. \tag{78}$$

For the smaller domain (78), instead of the sine expansion (77) it is convenient to use the odd cosine expansion

$$\cos\frac{\pi\phi}{2S},\quad \cos\frac{3\pi\phi}{2S},\ldots,\quad \cos\frac{(2n+1)\pi\phi}{2S},\ldots,$$

which takes care of both the symmetry condition at $\phi = 0$ and the zero Dirichlet condition at $\phi = S$.

Due to the singularity at $\boldsymbol{x} = \boldsymbol{0}$, convergence of the discrete fundamental solution to the continuous fundamental solution cannot be expected on the entire domain and rather needs to be assessed only some distance away from the origin. We first notice that the form of Eq. (71) suggests that

$$\max|G^{(h)}| = |G^{(h)}(0,0,0)| \propto \frac{1}{h}, \tag{79}$$

because on the left hand side of (71) we have division by h^2 inside $\Delta^{(h)}$. In our experiments we make sure that the scaling law (79) indeed holds and normalize the error accordingly:

$$\epsilon(i,j,k) \stackrel{\text{def}}{=} \frac{|G^{(h)}(i,j,k) - G(ih,jh,kh)|}{|G^{(h)}(0,0,0)|}. \tag{80}$$

In Table 1, we summarize the grid convergence results for the domain of size $S = 1$. We see that the normalized error (80) becomes smaller than a given threshold at a fixed number of cells away from the origin, which means that the actual distance at which it occurs decreases proportionally to h (columns 3 and 4 of Table 1). At the same time, from column 5 of Table 1 we see that at a fixed distance from the origin (half domain size) the error (80) decreases proportionally to h^3. If this error was not normalized by the quantity $\sim h^{-1}$, see formula (79), then it would have decreased proportionally to h^2 according with the accuracy of the scheme.

The discrete fundamental solution $G^{(h)}$ is translationally invariant. For a compactly supported RHS f on the grid, solution to the finite-difference Poisson equation [cf. formula (28)]

$$\Delta^{(h)}u = f \tag{81}$$

subject to the condition of decay at infinity is given by the discrete convolution (cf. formula (35)):

$$u(i,j,k) = \sum_{i',j',k'} G^{(h)}(i',j',k')f(i-i',j-j',k-k'). \tag{82}$$

Since far away from the origin (beyond the cube (75)) the discrete fundamental solution $G^{(h)}$ coincides with the continuous fundamental solution G, then the grid function u given by (82) vanishes at infinity. Moreover, if the discrete RHS f in Eq. (81) corresponds to a sufficiently smooth RHS of the continuous Poisson equation, then solution (82) will exhibit a conventional second order grid convergence on the entire domain of interest.

Table 1
Grid convergence of the discrete fundamental solution.

N	$\lvert G^{(h)}(0,0,0)\rvert$	$\max_{i,j}\epsilon(i,j,k) < 10^{-5}$	$\max_{i,j}\epsilon(i,j,k) < 10^{-6}$	$\max_{i,j}\epsilon(i,j,N/2)$
32	8.087389	$k = 20$	–	$0.189\cdot10^{-4}$
64	16.174784	$k = 20$	$k = 42$	$0.234\cdot10^{-5}$
128	32.349569	$k = 20$	$k = 43$	$0.292\cdot10^{-6}$
256	64.699138	$k = 20$	$k = 43$	$0.356\cdot10^{-7}$
512	129.398277	$k = 20$	$k = 43$	$0.456\cdot10^{-8}$

References

[1] H. Grad, H. Rubin, Hydromagnetic equilibria and force-free fields, in: Proceedings of the Second U.N. International Conference on the Peaceful uses of Atomic Energy, Geneva, Switzerland, vol. 3I, IAEA, Geneva, 1958, p. 190.
[2] V.D. Shafranov, Plasma equilibrium in a magnetic field, in: M.A. Leontovich (Ed.), Reviews of Plasma Physics, 2, Consultants Bureau, New York, NY, 1966, pp. 103–151.
[3] R.E. Peterkin Jr, M.H. Frese, C.R. Sovinec, Transport of magnetic flux in an arbitrary coordinate ALE code, J. Comput. Pgys. 140 (1) (1998) 148–171.
[4] U. Shumlak, T.W. Hussey, R.E. Peterkin Jr., Three-dimensional magnetic field enhancement in a liner implosion system, IEEE Trans. Plasma Sci. 23 (1) (1995) 83–88.
[5] J.N. Reddy, An Introduction to Finite Element Method, McGraw-Hill, New York, 1984.
[6] S.V. Tsynkov, Numerical solution of problems on unbounded domains. A review, Appl. Numer. Math. 27 (4) (1998) 465–532.
[7] A.P. Calderon, Boundary-value problems for elliptic equations, in: Proceedings of the Soviet-American Conference on Partial Differential Equations at Novosibirsk, Fizmatgiz, Moscow, 1963, pp. 303–304.
[8] R.T. Seeley, Singular integrals and boundary value problems, Amer. J. Math. 88 (1966) 781–809.
[9] V.S. Ryaben'kii, Boundary equations with projections, Russian Math. Surveys 40 (2) (1985) 147–183.
[10] V.S. Ryaben'kii, Method of Difference Potentials and Its Applications, Vol. 30 of Springer Series in Computational Mathematics, Springer-Verlag, Berlin, 2002.
[11] J. Lončarić, V.S. Ryaben'kii, S.V. Tsynkov, Active shielding and control of noise, SIAM J. Appl. Math. 62 (2) (2001) 563–596.
[12] S.V. Tsynkov, On the definition of surface potentials for finite-difference operators, J. Sci. Comput. 18 (2) (2003) 155–189.
[13] S.V. Utyuzhnikov, Generalized Calderón–Ryaben'kii potentials, IMA J. Appl. Math. 74 (1) (2009) 128–148.
[14] M. Medvinsky, S. Tsynkov, E. Turkel, The method of difference potentials for the Helmholtz equation using compact high order schemes, J. Sci. Comput. 53 (1) (2012) 150–193.
[15] A.N. Tikhonov, A.A. Samarskii, Equations of Mathematical Physics, Pergamon Press, Oxford, 1963.
[16] S.V. Tsynkov, External boundary conditions for three-dimensional problems of computational aerodynamics, SIAM J. Sci. Comput. 21 (1999) 166–206.
[17] P.M. Morse, H. Feshbach, Methods of Theoretical Physics. 2 Volumes, International Series in Pure and Applied Physics, McGraw-Hill Book Co., Inc., New York, 1953.
[18] U. Shumlak, J. Loverich, Approximate Riemann solver for the two-fluid plasma model, J. Comput. Phys. 187 (2) (2003) 620–638, http://dx.doi.org/10.1016/S0021-9991(03)00151-7. <http://www.sciencedirect.com/science/article/pii/S0021999103001517>.
[19] J. Loverich, U. Shumlak, A discontinuous Galerkin method for the full two-fluid plasma model, Comput. Phys. Commun. 169 (1G++3) (2005) 251–255, http://dx.doi.org/10.1016/j.cpc.2005.03.058. <http://www.sciencedirect.com/science/article/pii/S0010465505001554>.
[20] U. Shumlak, R. Lilly, N. Reddell, E. Sousa, B. Srinivasan, Advanced physics calculations using a multi-fluid plasma model, Comput. Phys. Commun. 182 (9) (2011) 1767–1770, http://dx.doi.org/10.1016/j.cpc.2010.12.048. <http://www.sciencedirect.com/science/article/pii/S001046551100004X>.
[21] L. Greengard, V. Rokhlin, A fast algorithm for particle simulations, J. Comput. Phys. 73 (2) (1987) 325–348.
[22] I. Tsukerman, A singularity-free boundary equation method for wave scattering, IEEE Trans. Antenn. Propag. 59 (2) (2011) 555–562.
[23] B.B. Kadomtsev, Collective Phenomena in Plasma (Kollektivnye yavleniya v plazme), 2nd Ed., Nauka, Moscow, 1988.
[24] D.B. Melrose, R.C. McPhedran, Electromagnetic Processes in Dispersive Media A Treatment Based on the Dielectric Tensor, Cambridge University Press, Cambridge, 1991.
[25] E.M. Lifshitz, L.P. Pitaevskii, Course of theoretical physics ''Landau–Lifshits''. vol. 10. Physical kinetics, Pergamon International Library of Science, Technology, Engineering and Social Studies, Pergamon Press, Oxford, 1981, translated from the Russian by J.B. Sykes and R.N. Franklin.
[26] J.P.H. Goedbloed, S. Poedts, Principles of Magnetohydrodynamics: With Applications to Laboratory and Astrophysical Plasmas, Cambridge University Press, Cambridge, UK, New York, 2004.
[27] J.P. Freidberg, Plasma Physics and Fusion Energy, Cambridge University Press, Cambridge, UK, 2007.
[28] J.P.H. Goedbloed, Advanced Magnetohydrodynamics: With Applications to Laboratory and Astrophysical Plasmas, Cambridge University Press, Cambridge, UK, 2010.
[29] Redmond Plasma Physics Laboratory. FRC Introduction. <http://depts.washington.edu/rppl/programs/frc_intro.html> (April 1998).
[30] T.P. Intrator, J.Y. Park, J.H. Degnan, I. Furno, C. Grabowski, S.C. Hsu, E.L. Ruden, P.G. Sanchez, J.M. Taccetti, M. Tuszewski, W.J. Waganaar, G.A. Wurden, S.Y. Zhang, Z. Wang, A high-density field reversed configuration plasma for magnetized target fusion, IEEE Trans. Plasma Sci. 32 (1) (2004) 152–160.
[31] S. Zhang, G.A. Wurden, T.P. Intrator, E.L. Ruden, W.J. Waganaar, C.T. Grabowski, R.M. Renneke, J.H. Degnan, High-density field-reversed configuration plasma for magnetized target fusion, IEEE Trans. Plasma Sci. 34 (2) (2006) 223–228.